

1 Global Eddy Subduction Carbon Pump from Argo 2 Floats

3 **Maxime Keutgen^{1,2}, Laure Resplandy^{1,3}, Mathieu A. Poupon^{1,2}**

4 ¹Department of Geosciences, Princeton University, Princeton, NJ, USA

5 ²Atmospheric and Oceanic Sciences Program, Princeton University, Princeton, NJ, USA

6 ³High Meadows Environmental Institute, Princeton University, Princeton, NJ, USA

7 **Key Points:**

- 8 • The eddy subduction pump is evaluated globally from Argo float data, with 1,333
9 particulate organic carbon subduction events identified.
- 10 • The eddy subduction pump peaks during springtime in hotspots of eddy kinetic
11 energy, linked to mixed layer and symmetric instabilities.
- 12 • The estimated global particulate organic carbon export flux below 200 m by the
13 eddy subduction pump is 0.05 [$<0.01\text{--}0.28$] Pg C yr⁻¹.

Corresponding author: Maxime K. De Greef, maximek@princeton.edu

Abstract

The eddy subduction pump, part of the biological pump, transports carbon-rich surface filaments downward via kilometer-scale turbulence in frontal regions, over days to weeks. Because of its spatial and temporal scales, this pump has been challenging to observe and quantify. Prior studies assessed the eddy subduction pump but were geographically limited. We introduce a detection algorithm identifying subduction events using collocated anomalies in apparent oxygen utilization, absolute salinity, and optical backscattering. We apply it to 126,591 biogeochemical Argo profiles collected by 941 floats. The algorithm identifies 1,333 carbon subduction events concentrated in springtime hotspots with eddy kinetic energy in the Southern Ocean and the subpolar North Atlantic. Our findings suggest that symmetric instabilities could play at least as big a role than mixed layer instabilities in generating subduction events. We estimate a global export flux of particulate organic carbon below 200 m of $0.05 [< 0.01-0.28] \text{ Pg C yr}^{-1}$. About two-thirds of this export occurs in the Southern Ocean (40%) and the North Atlantic (25%). Less than 25% of this flux enters water masses that remain isolated from the atmosphere for at least 50 years. Including dissolved organic carbon yields a total organic carbon export of $0.09 [0.01-0.51] \text{ Pg C yr}^{-1}$, less than 5% of the total organic carbon exported by the biological pump and an order of magnitude smaller than previous estimates. Although difficult to resolve in Earth system models, the eddy subduction pump appears to be a secondary term in global carbon budgets.

Plain Language Summary

Tiny algae called phytoplankton use sunlight to turn dissolved carbon dioxide into organic matter. Some of this carbon leaves the surface ocean, is transported into the interior ocean and eventually circles back to the surface ocean, decades to millennia later. This process is called the biological carbon pump and consists of multiple pathways. One pathway, the eddy subduction pump, occurs when swirling kilometer-scale eddies along ocean fronts push filaments of carbon-rich surface water downward. Because these events are small and short-lived, they have been difficult to observe. We use measurements from 941 robotic floats that drift, dive, and resurface, much like weather balloons for the ocean, to detect these events worldwide. Most occur in the Southern Ocean and the subpolar North Atlantic, especially in spring when surface waters are rich in organic carbon. The eddy subduction pump transports less than 5% of the ocean's total organic carbon export, and therefore accounts for a very small fraction of the total amount of carbon transported by the ocean.

1 Introduction

The biological carbon pump transfers carbon to the ocean interior, maintaining a vertical gradient in dissolved inorganic carbon (DIC), with higher concentrations at depth than at the surface. By reducing surface DIC, the biological pump maintains the ocean's capacity to absorb atmospheric carbon (Volk & Hoffert, 1985), regulating atmospheric carbon dioxide concentrations on seasonal to millennial timescales (DeVries, 2022). The surface to deep carbon gradient is sustained by all mechanisms that transport dissolved and particulate carbon of biological origin from the ocean surface to the interior (Frenger et al., 2024). The biological pump exports $10 \pm 5 \text{ Pg C yr}^{-1}$ of particulate organic carbon from the surface to the deep ocean (Boyd et al., 2019; Nowicki et al., 2022; Wang et al., 2023). Once viewed solely as the gravitational sinking of particles (Falkowski et al., 1998), the biological pump is now understood as a set of interdependent biophysical pumps operating across hours to decades and spanning kilometer to basin scales, including the physical transport of carbon through submesoscale eddies, large-scale circulation, the mixed layer ventilation and its restratification, and active transport through

63 vertical migration of organisms (Boyd et al., 2019; Nowicki et al., 2022; Siegel et al., 2023;
64 Poupon et al., 2025).

65 Among the various pumps that make up the biological carbon pump, the eddy sub-
66 duction pump remains one of the least well understood, with estimates ranging from 0
67 to 2 Pg C yr⁻¹ (Boyd et al., 2019). The eddy subduction pump is defined as a physi-
68 cally driven component of the biological carbon pump, involving the transport of carbon-
69 rich surface waters by the large vertical velocities associated with physical instabilities
70 at submesoscale (0.1-10 km) fronts (Omand et al., 2015; Lévy et al., 2024). Observations
71 with gliders and autonomous Argo floats have detected the eddy subduction pump in
72 specific oceanic regions, e.g., the North Atlantic, the Southern Ocean and the Kuroshio;
73 (Omand et al., 2015; Llort et al., 2018; S. Chen et al., 2021; Lacour et al., 2019; M. L. Chen
74 & Schofield, 2024). Yet, a global evaluation remains elusive because the eddy subduc-
75 tion pump is inherently episodic and localized, making it difficult to capture with sparse
76 observational coverage and challenging to extrapolate beyond regional studies. In ad-
77 dition, most previous studies have relied on region-specific detection algorithms, which
78 were tailored to local oceanographic conditions and therefore not directly transferable
79 to other regions (e.g. Omand et al., 2015; Llort et al., 2018; S. Chen et al., 2021; Lacour
80 et al., 2023). As a result, attempts at a global quantification of the eddy subduction pump
81 have been highly uncertain: early estimates extrapolated from observations in the North
82 Atlantic once suggested that the eddy subduction pump could export around 2 Pg C yr⁻¹,
83 about 20% of the biological carbon pump's export (Omand et al., 2015; Boyd et al., 2019).
84 However, more recent estimates based on observations in the Southern Ocean and an ide-
85 alized North Atlantic model place its contribution below 19% and 5%, respectively (Llort
86 et al., 2018; Resplandy et al., 2019).

87 Uncertainty in the magnitude of the eddy subduction pump arises from its strong
88 spatial and temporal variability. Seminal work by Omand et al. (2015) suggested that
89 the eddy subduction pump could operate across broad regions in the mid to high lat-
90 itudes, but subsequent regional studies indicate that the eddy subduction pump is in-
91 stead concentrated in a limited number of hotspots shaped by distinct dynamical char-
92 acteristics such as proximity to topographic features (Llort et al., 2018), high kinetic en-
93 ergy at frontal zones (S. Chen et al., 2021; Lacour et al., 2023) or seasonally deep mixed
94 layers (A. R. Johnson & Omand, 2021). Temporally, the picture is equally complex: while
95 some studies found enhanced activity of the eddy subduction pump in late winter to early
96 spring (Erickson & Thompson, 2018; S. Chen et al., 2021), others found that the eddy
97 subduction pump peaks in late spring or summer (Llort et al., 2018; A. R. Johnson &
98 Omand, 2021), and still others detected no clear seasonality at all (Lacour et al., 2023).
99 These conflicting findings reflect the limitations of regionally restricted studies and em-
100 phasize the need for a multi-year global assessment of the eddy subduction pump. How-
101 ever, such an assessment has so far been hindered by the absence of a globally applica-
102 ble detection algorithm as existing approaches relied on region-specific criteria tailored
103 to local dynamics (Llort et al., 2018; A. R. Johnson & Omand, 2021; Lacour et al., 2023;
104 M. L. Chen & Schofield, 2024). Overcoming this technical gap is essential to enable the
105 first robust quantification of the eddy subduction pump magnitude, seasonality, and con-
106 tribution to the biological carbon pump.

107 The mechanisms driving the eddy subduction pump remain debated. Eddy sub-
108 duction events are by-products of the restratification of submesoscale fronts (Taylor &
109 Thompson, 2023; Lévy et al., 2024), which in turn depend on both the processes that
110 generate fronts and the instabilities that restratify them. Fronts may emerge either be-
111 cause of spontaneous frontogenesis or forced frontogenesis (Hoskins & Bretherton, 1972;
112 Blumen, 2000; Shakespeare & Taylor, 2013), while fronts restratification is linked to in-
113 stabilities such as symmetric instabilities (Thomas et al., 2013; Bachman et al., 2017),
114 mixed layer instabilities (Boccaletti et al., 2007; Fox-Kemper et al., 2008), or a conjunc-
115 tion of both (Stamper & Taylor, 2017). Mixed layer instabilities are strongly modulated

116 by the mixed layer depth (MLD), while symmetric instabilities depend on the upper ocean
 117 water column stability and vertical stratification , which can be evaluated using the squared
 118 Brunt-Väisälä frequency (N^2). A global assessment of the eddy subduction pump would
 119 therefore also provide an opportunity to examine how dynamical conditions, such as mixed
 120 layer depth and water column stratification, shape the occurrence of the eddy subduc-
 121 tion pump, shedding light into the mechanisms at play.

122 In this study, we provide a global quantification of the eddy subduction pump and
 123 study its spatial and temporal variability. We build upon prior work that used subsur-
 124 face anomalies in data collected by autonomous platforms, such as gliders and Argo floats
 125 (Omand et al., 2015; Llort et al., 2018). We extend this approach by applying an algo-
 126 rithm that detects signatures of the eddy subduction pump to the global biogeochem-
 127 ical Argo float database (Bittig et al., 2019). In the following, section 2 presents the global
 128 biogeochemical Argo database, the global detection algorithm and the statistical meth-
 129 ods used to analyze the dataset. In section 3, we analyze the 1,333 detected carbon sub-
 130 duction events to identify spatial hotspots and assess the seasonality of the eddy sub-
 131 duction pump, as well as evaluate its potential physical and biological drivers. We es-
 132 timate the probability of a carbon subduction event across the world and the mean par-
 133 ticulate organic carbon content of carbon subduction events to provide a global carbon
 134 export of the eddy subduction pump. Finally, section 4 discusses how our global assess-
 135 ment of the eddy subduction pump confirms or challenges previous regional studies, and
 136 we discuss the small estimated range for the eddy subduction pump (0.05 [$< 0.01\text{-}0.28$]
 137 Pg C yr $^{-1}$) and its implications in the context of global carbon pump estimates.

138 2 Materials and Methods

139 2.1 Global Biogeochemical Argo Database

140 We used the 941 floats from the global biogeochemical Argo database (Wong et al.,
 141 2020; Bittig et al., 2019), equipped with sensors measuring salinity, temperature, oxy-
 142 gen, and particle backscattering at 700 nanometers (bbp₇₀₀). The dataset spans from
 143 May 2010 to May 2024. We retrieved the float metadata and individual profiles using
 144 the OneArgo-R toolbox (Cornec et al., 2022), which provides access to the global index
 145 of available biogeochemical floats. The 941 selected floats yielded a total of 126,591 pro-
 146 files, an order of magnitude more than the combined number of profiles analyzed in prior
 147 regional studies of the eddy subduction pump (Llort et al., 2018; A. R. Johnson & Omand,
 148 2021; S. Chen et al., 2021; Lacour et al., 2023; M. L. Chen & Schofield, 2024). For each
 149 profile, we detected signatures of the eddy subduction pump using salinity, apparent oxy-
 150 gen utilization, and particle backscattering at 700 nanometers to detect subduction events
 151 (see sections 2.2). Additionally, for subsequent analysis, we computed the maximum Brunt-
 152 Väisälä frequency across the water column as a proxy for vertical stratification. We also
 153 estimated the mixed layer depth using the standard density threshold method, defined
 154 as the depth where the potential density exceeds the surface value by more than 0.03 kg m $^{-3}$
 155 (de Boyer Montégut et al., 2004; Kelley et al., 2024).

156 The spatial coverage of the selected floats is uneven: only 33% of 1°x1° ocean grid
 157 cells contain at least one profile, meaning that even at the mesoscale, approximately two-
 158 thirds of the global ocean remain unsampled, see Figure S1 in the supplementary infor-
 159 mation (SI). Data coverage is densest in regions such as the North Atlantic, the South-
 160 ern Ocean, the northern Indian Ocean, and the Kuroshio Extension, where many 1x1°
 161 grid cells contain more than 25 profiles, and in some cases, over 100. In contrast, large
 162 areas are undersampled, including the southwestern Gulf Stream, most of the Pacific (par-
 163 ticularly the tropics), parts of the Kuroshio Extension, the South Atlantic, and the south-
 164 ern Indian Ocean, where grid cells generally contain fewer than 5 profiles. Notably, be-
 165 cause of sea ice, the Arctic Ocean lacks Argo profiles entirely.

166 **2.2 Subduction Events Definition**

167 Building on previous methods for detecting subduction events (Llort et al., 2018;
 168 S. Chen et al., 2021; K. S. Johnson et al., 2017; Lacour et al., 2023; M. L. Chen & Schofield,
 169 2024), we define two types of events that can be identified using the Argo float database:
 170 *physical subduction events* and *carbon subduction events*. *Physical subduction events* are
 171 defined as colocated subsurface negative anomalies in apparent oxygen utilization (AOU),
 172 defined as the difference between oxygen solubility and measured oxygen, and positive
 173 or negative anomalies relative to the vertical background in salinity (S), but not nec-
 174 essarily an anomaly in bbp_{700} (Figure 1). *Carbon subduction events* are a subset of phys-
 175 ical subduction events, marked by the same AOU and salinity anomalies but with an ad-
 176 ditional positive anomaly in bbp_{700} , a proxy for particulate organic carbon (POC). This
 177 classification reflects the idea that a parcel of near-surface water injected into the ocean
 178 interior via subduction will carry surface-like properties—namely, elevated salinity, higher
 179 oxygen concentrations (i.e., lower AOU), and possibly elevated POC relative to surround-
 180 ing waters. Such intrusions appear as local extrema relative to the background vertical
 181 structure (Figure 1).

182 While previous studies have used spiciness, which is a weighted combination of tem-
 183 perature and salinity (McDougall & Krzysik, 2015), to detect water mass intrusions (Llort
 184 et al., 2018; S. Chen et al., 2021; M. L. Chen & Schofield, 2024), we opt for salinity in-
 185 stead. Salinity is a conservative tracer and has been shown to perform as well as, or bet-
 186 ter than, spiciness in identifying water masses (McDougall et al., 2021; Tailleux, 2021).
 187 In the context of subduction event detection, salinity proves more robust because it is
 188 unaffected by temperature diffusion. Spiciness anomalies, by contrast, may be diminished
 189 if the associated temperature signal dissipates before the subduction event is captured
 190 by the float. An example of this effect is shown in Figure S2 in the SI. Thus, using salin-
 191 ity reduces the likelihood of false negatives (i.e., cases where subduction events occur but
 192 go undetected).

193 **2.3 Subduction Events Detection Algorithm**

194 Prior work detecting subduction events was tailored to specific ocean regions (e.g.
 195 the Southern Ocean, the Kuroshio extension, and the North Atlantic) and could not be
 196 used at the global scale (Llort et al., 2018; S. Chen et al., 2021; M. L. Chen & Schofield,
 197 2024). Here, we expand this work and develop a statistical algorithm to detect the foot-
 198 prints of subduction events that works for the global ocean (? , ?). The algorithm scans
 199 each Argo profile vertically and, at each depth below 200 m, looks for negative anom-
 200 alies in AOU, positive anomalies in bbp_{700} , and positive or negative anomalies in abso-
 201 lute salinity. Note that we do not use the top 200 m to detect physical and carbon sub-
 202 duction events because the primary goal of this study is to evaluate the impact of car-
 203 bon subduction on the eddy pump below a fixed depth horizon of 200 m, which is a depth
 204 that is deeper than the seasonally varying mixed layer depth in most of the ocean (de
 205 Boyer Montégut et al., 2004).

206 The main difference with prior work is that we replace the cutoffs tailored to spe-
 207 cific ocean regions with a robust residuals-based approach that can be applied globally.
 208 Anomalies in AOU, salinity, and bbp_{700} are identified by comparing each measurement
 209 to a robust estimate of the background vertical trend. In practice, we compute a 3-bin
 210 moving average and subtract a robust 9-bin trimmed mean to obtain the anomaly sig-
 211 nal. The trimmed mean is an estimate of the mean of a random variable which is less
 212 sensitive to outliers than the arithmetic mean (Huber, 2004). The difference between the
 213 3-bin moving average and the 9-bin trimmed mean is then standardized using a robust
 214 estimator of variance, the normalized interquartile range, an estimator of the standard
 215 deviation of a random variable which is also less sensitive to outliers than the sample stan-

216 dard deviation (Rousseeuw & Hubert, 2018). This procedure yield robust standardized
 217 residuals.

218 Observations with a standardized residual exceeding approximately 2σ (97.5th percentile
 219 of a standard normal distribution) for AOU and salinity and 1σ (68th percentile)
 220 for bbp700 are flagged as *carbon subduction events* (Figure 1). The lower threshold for
 221 bbp700 is used because of its relatively higher noise level. Data points meeting the residual
 222 criteria for AOU and salinity but not for bbp700 are classified as *physical subduc-*
 223 *tion events*. Lastly, we verify that the finite-difference approximation of the first deriva-
 224 *tive changes sign within ± 100 m of the detected level; this ensures that the detected level*
 225 *represents local extremes in AOU, salinity, and bbp700, thereby improving the algorithm's*
 226 *specificity (see algorithm S1 in the SI for details).*

227 We tuned the detection algorithm toward high sensitivity to minimize missed events,
 228 prioritizing the reduction of false negatives over the reduction of false positives. In prac-
 229 tice, it is preferable to flag many potential events, including false positives that can later
 230 be discarded by inspection, rather than risk missing true subduction events. Of the 9,979
 231 anomalies flagged by the algorithm, manual inspection confirmed 4,377 true positives and
 232 rejected 5,602 false positives according to the following criteria: colocated AOU and salin-
 233 ity peaks clearly identifiable by eye, situated below the mixed layer, with a vertical ex-
 234 tent smaller than 200 m. To quantify the false-negative rate, we randomly selected 1,000
 235 profiles from nine floats and manually classified every profile they recorded. The algo-
 236 rithm correctly detected 92% of genuine physical subduction anomalies, corresponding
 237 to a false-negative rate of about 8%, which we considered acceptable. Thresholds were
 238 chosen after exploratory tests showed that stricter cutoffs (e.g., $> 2\sigma$) eliminated many
 239 genuine anomalies, whereas looser ones ($< 1\sigma$) produced an unmanageable number of
 240 false positives. In the end, the algorithm, combined with manual verification, yielded 4,377
 241 true physical subduction events and 1,333 true carbon subduction events.

242 **2.4 Probability of Subduction and Global Statistical Interpolation**

243 The detection algorithm and the subsequent manual verification give the spatial
 244 and temporal location of physical and carbon subduction events and reflect the uneven
 245 coverage of the Argo database. Thus, more subduction events are detected in well-sampled
 246 regions (Figure 2a-b). To take this sampling bias into account, we perform a statistical
 247 interpolation that allows us to more reliably identify hotspots of physical/carbon sub-
 248 duction. We grid the data in $1^\circ \times 1^\circ$ grid cells, and consider the proportion p_i of y_i phys-
 249 ical or carbon subduction events detected in grid cell i to N_i , the total number of Argo
 250 profiles in the grid cell i : $p_i = y_i/N_i$.

251 The random quantity p_i lends itself to a straightforward interpretation: in the limit
 252 where the number of Argo profiles in a grid cell is sufficiently large, this is the proba-
 253 bility that an Argo float present in that grid cell captures a physical or carbon subduc-
 254 tion event. However, the computed values p_i are still exposed to a bias, as grid cells with
 255 very few total numbers of Argo profiles (N_i) are likely to have an unrealistically high or
 256 low estimated p_i by chance. Therefore, we fit statistical generalized additive models (GAMs),
 257 with spherical splines to account for Earth's spherical geometry (Wahba, 1981), to in-
 258 terpolate p_i and produce smoothed maps of the average probability that an Argo float
 259 contains physical subduction events and carbon subduction events, we refer to this in-
 260 terpolated average probability as \hat{p}_i . We take into account the bias introduced by grid
 261 cells with few Argo profiles by weighting observations i by $\log(N_i)$, such that the fitted
 262 models gives more weight to more reliable observations, i.e. with a higher number of Argo
 263 profiles in the grid cells. The GAMs are optimized to explain at least 60% of the model
 264 deviance (Hastie & Tibshirani, 1986), balancing model complexity and goodness of fit.
 265 We then interpolate the fitted model onto a finer 0.25° grid to produce smooth maps of

266 the probability of physical subduction and of carbon subduction (Wahba, 1981; Hastie
267 et al., 2001). See details on the estimation of GAMs in text S1 in SI.

268 2.5 Eddy Kinetic Energy and Turnover Time Datasets

269 To assess the relationship between subduction events and mesoscale eddy activity,
270 we used both balanced eddy kinetic energy (EKE), reflecting low-frequency, geostrophically
271 balanced mesoscale eddies and fronts and unbalanced eddy kinetic energy, reflecting
272 high-frequency, ageostrophic internal tides and internal-gravity/near-inertial waves
273 (Qiu et al., 2018). Balanced and unbalanced EKE measurements are derived from high-
274 resolution 1/48° MITgcm simulations by Qiu et al. (2018). Balanced and unbalanced eddy
275 kinetic energy are defined for a given horizontal wavenumber k_h as

$$\text{KE}_{\text{bal}}(k_h) = \int_{\omega_{yr}}^{\omega_{cr}} \hat{E}(k_h, \omega) d\omega , \quad \text{KE}_{\text{unbl}}(k_h) = \int_{\omega_{cr}}^{\omega_{Ny}} \hat{E}(k_h, \omega) d\omega , \quad (1)$$

276 where $\text{KE}_{\text{bal}}(k_h)$ represents the balanced kinetic energy integrated in wave number space
277 from the yearly frequency (ω_{yr}) to the critical frequency (ω_{cr}) and $\text{KE}_{\text{unbl}}(k_h)$ corresponds
278 to the unbalanced kinetic energy integrated from the critical frequency (ω_{cr}) to the Nyquist
279 frequency (ω_{Ny}). The critical frequency is defined as the minimum of either the local
280 tenth vertical-mode internal gravity wave dispersion frequency or the permissible tidal
281 frequencies (Qiu et al., 2018).

282 The high-resolution EKE fields were spatially averaged onto a 0.25° grid to facilitate
283 comparison with our 0.25°-resolution dataset representing the probability of physical
284 subduction. To quantify the association between EKE and subduction probability,
285 we fitted generalized linear models (GLMs) across two latitudinal bands: the tropics (30°S
286 to 30°N) and the extratropics (latitudes greater than 30° N or 30° S). Further methodological
287 details are provided in Text S2 of the SI.

288 We also used the dissolved inorganic carbon reemergence time fields of Siegel et al.
289 (2021). The reemergence time is defined as the time necessary for the water masses to
290 return to the surface. The data product is provided on a 2° horizontal grid with 48 vertically
291 irregular layers. We applied nearest-neighbor interpolation to collocate these fields
292 with our grid and, for each season, estimated the fraction of POC exported by the eddy
293 subduction pump below 200 m that is expected to remain out of contact with the atmosphere
294 for at least 50 years. Following Frenger et al. (2024); Visser (2025), we avoid the term "sequestration timescale" for DIC and instead use "reemergence time" to emphasize
295 that this metric reflects ventilation/return to the surface rather than net offset
296 of anthropogenic emissions.

298 2.6 Quantification of Carbon Export from Carbon Subduction Events

299 We estimate the contribution of each carbon subduction event to the eddy subduction
300 pump by computing the local flux below 200 meters of particulate organic carbon
301 (POC) attributable to these events for each season and each 0.25° grid cell. This estimation
302 proceeds in several steps. First, for each detected carbon subduction event, we
303 convert bbp_{700} profiles to POC concentrations (in mg C m^{-3}) using the algorithm developed
304 by Galí et al. (2022) (see Text S3 in the SI for details). We then estimate the POC anomaly
305 associated with the event by computing the depth-integrated deviation from a background profile
306 (Figure 1c). Specifically, we define the anomaly as the difference between the observed POC
307 concentration, $\text{POC}^{\text{obs}}(z)$, and a linear background profile, $\text{POC}^{\text{lin}}(z)$, interpolated between the nearest local extrema above (z_1) and below (z_2)
308 the anomaly within a 300 m window

$$\text{POC}_{\text{int}} = \int_{z_1}^{z_2} (\text{POC}^{\text{obs}}(z) - \text{POC}^{\text{lin}}(z)) dz \quad [\text{mg C m}^{-2}] . \quad (2)$$

310 Dividing the inventory of excess particulate carbon contained in a subducted filament
 311 POC_{int} by the export horizon H converts that inventory to an average concentration anomaly
 312 over the depth range where export of the eddy subduction pump is presumed to occur.

313 To obtain spatially continuous maps, we fit a generalized additive model to POC_{int} ,
 314 yielding seasonal interpolated fields of the depth-integrated POC anomaly across the 0.25°
 315 grid (see Figure S3 in the SI). We consider POC_{int} to be the inventory of excess partic-
 316 ulate carbon contained in a subducted filament. This approach parallels the generalized
 317 additive model interpolation of the probability of carbon subduction events, p presented
 318 in section 2.4 (see Text S1 for details).

319 Next, we use the interpolated fields of integrated POC anomaly (POC_{int}) to esti-
 320 mate the local daily POC flux, Q , attributable to the eddy subduction pump:

$$321 Q = \text{POC}_{\text{int}} \times \frac{W}{H} \times \hat{p} \quad [\text{mg C m}^{-2} \text{ d}^{-1}], \quad (3)$$

322 where W is the characteristic vertical velocity of subduction (in m d^{-1}), $H = 200 \text{ m}$
 323 is the assumed depth of the export horizon, and \hat{p} is the interpolated seasonal probabili-
 324 ty of detecting a carbon subduction event. The average concentration anomaly POC_{int}
 325 is multiplied by the characteristic vertical velocity of subduction W yields the advective
 326 flux associated with a single event. Lastly, \hat{p} , scales this single-event flux by the seasonal
 327 probability of a carbon subduction event, producing a local daily flux for each grid cell
 and each season.

328 Additionally, we account for the possibility that the integrated POC anomaly (POC_{int})
 329 observed by Argo floats may underestimate the total amount originally subducted, due
 330 to remineralization during the time lag between subduction and detection. Following A. R. John-
 331 son and Omand (2021), who reported subduction anomalies persisting for up to three
 332 months, we therefore apply a high-bound exponential correction assuming an e -folding
 333 decay timescale of 90 days. Specifically, we multiply POC_{int} by e to obtain an upper-
 334 bound estimate of the original anomaly such that Q may be upper-bounded as

$$335 Q^+ = e \times \text{POC}_{\text{int}} \times \frac{W}{H} \times \hat{p} \quad [\text{mg C m}^{-2} \text{ d}^{-1}]. \quad (4)$$

336 The impact of this correction is also included in the sensitivity analysis shown in Fig-
 ure S5.

337 In addition, using the interpolated reemergence time product of Siegel et al. (2021),
 338 we estimate for each seasonal flux Q and its upper-bound Q^+ , the mean fraction of the
 339 exported carbon that will be trapped into water masses that remains out of contact with
 340 the atmosphere for at least 50 years, this yields $Q_{50 \text{ yrs}}$ and $Q_{50 \text{ yrs}}^+$.

341 Lastly, the global annual export attributable to the eddy subduction pump and ex-
 342 pressed in Pg C yr^{-1} is then obtained by integrating Q or its upper-bound Q^+ over the
 343 ocean's surface and over seasons. In addition, the fraction of that global annual export
 344 that happens in water masses that remain sequestered for more than 50 years is also ob-
 345 tained by integrating $Q_{50 \text{ yrs}}$ and its upper-bound $Q_{50 \text{ yrs}}^+$.

346 The limitations and assumptions behind this method are as follows.

- 347 • Constant depth of the export horizon (H). The assumption of constant depth of
 348 the export horizon H assumes that the relevant export horizon of the eddy sub-
 349 duction pump is 200 meters. However, shallower export in the tropics (lower H)
 350 or deeper export in the subpolar gyres (higher H) would lead to under- or over-
 351 estimation, respectively.
- 352 • Uniform characteristic velocity (W). Here, we use $W = 200 \text{ m d}^{-1}$ as a repre-
 353 sentative mid-range value, consistent with observational estimates of submesoscale
 354 dynamics (Torres et al., 2024; Zhu et al., 2024), but also include the sensitivity

- 355 to a plausible range for vertical velocities between 20 and 500 m d⁻¹ (Stamper
 356 & Taylor, 2017) to provide a first-order uncertainty envelope for our eddy pump
 357 flux estimate. The sensitivity of Q to W is shown in Figure S5 in SI.
- 358 • Event independence. We assume event independence in computing \hat{p} . However,
 359 in regions where subduction clusters in space or time, this assumption may inflate
 360 the effective frequency of individual carbon subduction events and therefore over-
 361 estimate of the local daily flux.
 - 362 • Stationarity of the probability of carbon subduction within each season. In equa-
 363 tion 3, we multiply by \hat{p} , which is fixed for each season. However, the probabili-
 364 ty of carbon subduction is likely to be highly dependent on intraseasonal dynam-
 365 ics such as wind speed or sea surface temperature and salinity, affecting front for-
 366 mation and eventually, subduction.
 - 367 • Neglect of lateral diffusion
 - 368 • Potential exponential-decay of the POC signal with time (see equation 4)

369 In the discussion section (section 4), we discuss the impact of the limitations here-above
 370 on our assessment of the eddy subduction pump.

371 2.7 Statistical metrics

372 We conducted hypothesis tests to assess the statistical significance of seasonal vari-
 373 ability in both the frequency and the depth of subduction events. This step is essential
 374 given the uneven spatial and temporal sampling of the Argo float database.

375 To test whether the occurrence of carbon and physical subduction events exhibits
 376 significant seasonality, we evaluated the null hypothesis that normalized monthly detec-
 377 tion probabilities are uniformly distributed. For each month i , the normalized detection
 378 probability \hat{p}_i is defined as

$$\hat{p}_i = \frac{p_i}{\sum_{k=1}^{12} p_k}, \quad (5)$$

379 where p_i is the raw monthly probability. Under the null hypothesis, \hat{p}_i follow a uniform
 380 distribution $U(1/12)$, and deviations from uniformity were assessed using a χ^2 goodness-
 381 of-fit test. Because tests were applied separately to multiple ocean regions, we controlled
 382 the family-wise error rate using a Bonferroni correction, setting the adjusted significance
 383 threshold to $\alpha = 0.05/5 = 0.01$ (VanderWeele & Mathur, 2019).

384 To examine whether the vertical extent of subduction events also varies seasonally,
 385 we applied a Kruskal-Wallis test to the monthly distributions of subduction depths. The
 386 test was performed on both the full set of detected events and on the subset compris-
 387 ing the deepest 20% of events (i.e., the top quintile).

388 3 Results

389 3.1 Spatial Distribution of Physical and Carbon Subduction

390 Primary hotspots of physical subduction, where the annual probability of subduc-
 391 tion exceeds 30 %, are detected in the subpolar North Atlantic, the equatorial Indian
 392 Ocean and in the Southern Ocean, specifically, between the Subantarctic Front and the
 393 Southern ACC Front, downstream of the Drake Passage and of the Kerguelen Plateau,
 394 south of New Zealand, near the East Pacific Antarctic Ridge and in the Agulhas current
 395 (Figure 2a,b). Secondary hotspots, where the annual probability of physical subduction
 396 is 10-30%, are found in the Mediterranean Sea, the Kuroshio and California Currents.
 397 Secondary hotspots are also detected in the equatorial Pacific and equatorial Atlantic,
 398 but these areas are poorly sampled by Argo floats, limiting confidence in the magnitude
 399 and spatial extent of these features (red dots in Figure 2c,d).

Hotspots of carbon subduction are less numerous than hotspots of physical subduction, and are primarily concentrated at mid- to high-latitude in the Southern Ocean and subpolar North Atlantic (Figure 2f,g). Primary hotspots of carbon subduction, where the annual probability of carbon subduction is over 10% are detected in the North Atlantic and the Southern Ocean downstream of the Drake Passage, and along the Pacific-Antarctic Ridge, while secondary carbon subduction hotspots, with probabilities between 2.5 and 10 %, are detected in the Agulhas Current, downstream of the Kerguelen Plateau, south of New Zealand, in the Indian Ocean, and in the Eastern Pacific. Like for physical subduction, the equatorial Eastern Pacific, Indian Ocean, and equatorial Atlantic also contain weak hotspots, but the confidence in these hotspots is lower due to limited sampling Argo coverage (red dots in Figure 2c,d).

3.2 Seasonality of Physical and Carbon Subduction

We evaluate the seasonality of physical and carbon subduction events at regional scale, and find higher subduction probabilities and stronger seasonality in the Southern Ocean and the North Atlantic than in the North Pacific, the Northern Tropics and the Southern Tropics (barplots in Figure 3). In both the Southern Ocean and the North Atlantic, the probability of physical subduction rises from 4-5% in winter to about 7% in spring/summer, and the probability of carbon subduction doubles from 1-1.5% in winter to 3% in spring (peak in September-October in the Southern Ocean and April-May in the North Atlantic). The winter-to-spring increase in carbon subduction departs significantly from a uniform distribution in both regions (Southern Ocean: $\chi^2 = 28.5, p = 2.7 \times 10^{-3}$, North Atlantic: $\chi^2 = 35.9, p = 1.8 \times 10^{-4}$), while the seasonal increase in physical subduction is only statistical significant in the Southern Ocean (Southern Ocean: $\chi^2 = 40.3, p = 3.2 \times 10^{-5}$, North Atlantic: $\chi^2 = 19.4, p = 0.054$). In both regions, the spring peak in carbon subduction coincides with the seasonal mixed layer restratification and the seasonal rise in chlorophyll (blue and green lines in Figures 3f-g).

In contrast, in the North Pacific, Northern Tropics, and Southern Tropics, subduction probabilities are lower and seasonality is weaker. Across these regions, physical subduction probabilities remain between 1.5 and 3%, while carbon subduction is generally below 1% (average $\sim 0.3\%$), with modest peaks in summer in the Northern Tropics (August) and fall in the North Pacific (November). None of these seasonal fluctuations are statistically significant (North Pacific: $\chi^2 = 8.0, p = 0.71$; Northern Tropics: $\chi^2 = 18.9, p = 0.068$; Southern Tropics: $\chi^2 = 18.2, p = 0.077$). The lack of statistical significance should not be interpreted as proof that seasonality is absent, but that observations are too limited to draw firm conclusions about the presence or absence of seasonality

3.3 Depth of Physical and Carbon Subduction Events

Globally, 70-80% of physical and carbon subduction events lie between 200 m and 500 m (Figure 4). Note that by design, no events are detected above 200 m. For both carbon and physical subduction, depth distributions vary across basins. Subduction events reach greater depths in the Southern Ocean, North Atlantic, and Southern Tropics, where about 30% of physical subduction and 20% of carbon subduction events extend below 500 m (Figure 4). In contrast, events are generally shallower in the Northern Tropics and the North Pacific, with only about 20% and 7% of physical subduction events and 7% to none of carbon subduction events occurring deeper than 500 m (Figure 4). These observed patterns do not imply that carbon subduction cannot occur below 500 m in the Pacific, or that a third of physical subduction truly happens at depth below 500 meters. Rather, sparse Argo coverage and the intrinsic rarity of deep carbon and physical subduction make such events easy to miss and the small number of detected events increases sampling error. Within each region we detect no statistically significant seasonal shift in either the mean event depth or the thickness of the distribution tail.

451 **3.4 Potential Drivers of Physical Subduction**

452 We first assess whether subduction aligns with the two pathways of frontogenesis:
 453 forced frontogenesis or spontaneous frontogenesis (see section 1). To this end, we use the
 454 balanced and unbalanced EKE product as provided by Qiu et al. (2018) modeling product
 455 (see section 2.5). Balanced EKE is a proxy for persistent mesoscale strain that drives
 456 forced frontogenesis, while unbalanced EKE (internal tides and near-inertial waves) en-
 457 ergizes high-frequency shear that can either sharpen or weaken fronts episodically (Hoskins
 458 & Bretherton, 1972; Blumen, 2000; Shakespeare & Taylor, 2013).

459 In the extratropics (poleward of 30°), high balanced EKE is strongly associated with
 460 high probability of physical subduction (Figure 5a). Indeed, the odds of observing a sub-
 461 duction event rise sharply with balanced EKE, with a one-unit increase in the natural
 462 logarithm of balanced EKE, equivalent to multiplying balanced EKE by $e \approx 2.7$, boosts
 463 the odds of subduction by roughly 55 % (odds ratio, OR = 1.55; p-value $< 10^{-15}$).
 464 In the tropics (equatorward of 30°), however, the odds of observing a physical subduc-
 465 tion event declines with balanced EKE (OR = 0.92, p-value $< 10^{-15}$) with the odds
 466 of a physical subduction event (Figure 5).

467 By contrast, high unbalanced EKE is strongly negatively associated with the prob-
 468 ability of physical subduction in both the tropics and the extratropics. A one-unit in-
 469 crease in the natural logarithm of unbalanced EKE decreases the odds of subduction by
 470 roughly 21 % (OR = 0.79; p-value $< 10^{-15}$) in the extratropics and 45 % in the trop-
 471 ics (OR = 0.79, p-value $< 10^{-15}$), see figure 5. The strong link between subduction
 472 and balanced EKE suggest that subduction occurs in region of forced frontogenesis. In
 473 contrast, the reduction in subduction probability in regions of high unbalanced EKE sug-
 474 gest that internal tides and near inertial-waves suppress the occurrence of subduction
 475 (Hoskins & Bretherton, 1972; Blumen, 2000; Shakespeare & Taylor, 2013).

476 We also assess whether detected subduction events are more likely to be associated
 477 with mixed layer instabilities or symmetric instabilities. Deeper mixed layers are typ-
 478 ically associated with mixed layer instabilities, while lower values of N_{\max}^2 are linked to
 479 symmetric instabilities. To evaluate how water-column structure modulates subduction,
 480 we compare the median MLD and the median N_{\max}^2 between profiles with and without
 481 detected subduction (Figures 5b-c). Vertical stratification (N^2) is significantly and ro-
 482 bustly lower in profiles with subduction (median = 2.2×10^{-4} , IQR = 6.0×10^{-4}) than
 483 in profiles without subduction (median = 4.8×10^{-4} , IQR = 1.0×10^{-3} ; Figure 5c,d).
 484 In contrast, the mixed layer depth distributions of the profiles with and without subduc-
 485 tion are more similar. Profiles with subduction have somewhat deeper mixed layers (me-
 486 dian 59.6 m, IQR 87.6 m) than those without subduction (median 44.3 m, IQR 67.1 m),
 487 but the overlap between the two distributions is large (see Figure 5). Quantitatively, the
 488 Kolmogorov-Smirnov (KS) distance between the N_{\max}^2 distributions with and without
 489 subduction is twice that for MLD ($D = 0.22$ for N_{\max}^2 vs. $D = 0.11$ for MLD). We
 490 assessed whether this difference could arise from sampling error due to the limited num-
 491 ber of profiles by bootstrapping the calculation of KS distances. In 100% of 1,000 boot-
 492 strapped samples, the KS distance for N_{\max}^2 exceeds that of MLD, allowing us to reject
 493 the null hypothesis that the observed difference is due to chance. This stronger discrim-
 494 inatory power of N_{\max}^2 suggests that symmetric instability contribute at least as much
 495 as mixed layer instabilities to the occurrence of physical subduction events.

496 **3.5 Global and Regional Export of the Eddy Subduction Pump**

497 We evaluate the POC export below 200 meters (see details in section 2.6). Export
 498 fluxes are higher in the North Atlantic and the Southern Ocean where they reaches around
 499 5 [0.5, 50] mg C m $^{-2}$ d $^{-1}$, while they generally remain below 1.0 [0.1,5] mg C m $^{-2}$ d $^{-1}$
 500 in other regions (Figure 6b). These regional differences in fluxes arise from both the mean
 501 amount of POC subducted during each event (i.e., integrated POC anomalies) and the

frequency of these events (i.e., the probability of carbon subduction) which are both higher in the North Atlantic and the Southern Ocean than elsewhere (Figure 2d and Figure S3). Yet we note systematic differences between the two basins. The North Atlantic is characterized by higher POC content per event (more than 150 mg C m^{-2} in boreal summer) than the Southern Ocean (100 mg C m^{-2} in austral summer) leading to stronger local fluxes (Figure 6b and S3). The Southern Ocean is characterized by more hotspots than the North Atlantic, leading to a greater export flux when aggregated at basin scale (Figure 6a).

Integrated globally, we find a POC export flux associated with the eddy subduction pump of $0.05 [<0.01\text{--}0.28] \text{ Pg C yr}^{-1}$. The central estimate assumes a velocity of 200 m d^{-1} , whereas the lower and upper estimates assume velocities of 20 m d^{-1} and 500 m d^{-1} , respectively (see Sections 2.6 and 4.5). The Southern Ocean contributes about 40% to this global flux ($\sim 0.02 [0.002\text{--}0.11] \text{ Pg C yr}^{-1}$), the North Atlantic about 25% ($\sim 0.01 [0.001\text{--}0.08] \text{ Pg C yr}^{-1}$), and the North Pacific together with the Tropics the remaining 35% ($\sim 0.018 [0.002\text{--}0.09] \text{ Pg C yr}^{-1}$; Figure 6b).

We evaluate the fraction of global export occurring in water masses estimated to remain out of contact with the atmosphere for more than 50 years, using the reemergence time product of Siegel et al. (2021). This fraction is estimated at $0.014 [0.001\text{--}0.07] \text{ Pg C yr}^{-1}$ (Figure 6a). When restricting to waters isolated from the atmosphere for over 50 years, the relative contribution of the North Atlantic decreases from about 25% to 20% ($\sim 0.002 \text{ Pg C yr}^{-1}$), while the Southern Ocean remains near 40% ($\sim 0.006 \text{ Pg C yr}^{-1}$) and the North Pacific and Tropics rise from 35% to 40% ($\sim 0.006 \text{ Pg C yr}^{-1}$). The Mediterranean contributes around 3% of the total flux ($\sim 0.002 \text{ Pg C yr}^{-1}$), but less than 1% of the export that remains isolated for more than 50 years, pointing to shallower subduction in the Mediterranean compared to other regions (see Table S1 in the SI).

4 Discussion

4.1 Carbon Subduction Concentrated in Hotspots

In this study, we used the global biogeochemical Argo database to provide the first worldwide assessment of the eddy subduction pump. We developed a statistical framework to detect physical and carbon subduction events, allowing us to estimate a global POC export flux of $0.05 [<0.01\text{--}0.28] \text{ Pg C yr}^{-1}$. A central innovation is the use of the global biogeochemical Argo database to assign carbon subduction probabilities regionally, which reveals where the pump is most active. Primary hotspots (probability of carbon subduction more than 10 %) emerge in the subpolar North Atlantic, Drake Passage, and along the Pacific–Antarctic Ridge, while secondary hotspots (probability of carbon subduction between 2.5 % and 10 %) appear in the Agulhas Current, Kerguelen Plateau, and tropical Indian Ocean. Most export is sustained by springtime activity in regions of high eddy kinetic energy, especially in the Southern Ocean and subpolar North Atlantic. The locations of carbon subduction hotspots broadly align with earlier regional studies in the Southern Ocean (Llort et al., 2018; Lacour et al., 2023; M. L. Chen & Schofield, 2024), North Atlantic (A. R. Johnson & Omand, 2021), Kuroshio (S. Chen et al., 2021), Mediterranean (Mahadevan et al., 2020), and California Current (Stukel et al., 2017, 2018), while also highlighting previously unreported hotspots in the tropical Indian and Pacific Oceans.

4.2 Eddy Subduction Pump Peaks in Spring

The eddy subduction pump peaks in spring in well-sampled extratropical regions, including the North Atlantic and the Southern Ocean, whereas no significant seasonality is detected in the tropics. The absence of seasonality in the tropics likely reflects weaker submesoscale activity (Dong et al., 2021), lesser seasonality of the mixed layer depth and

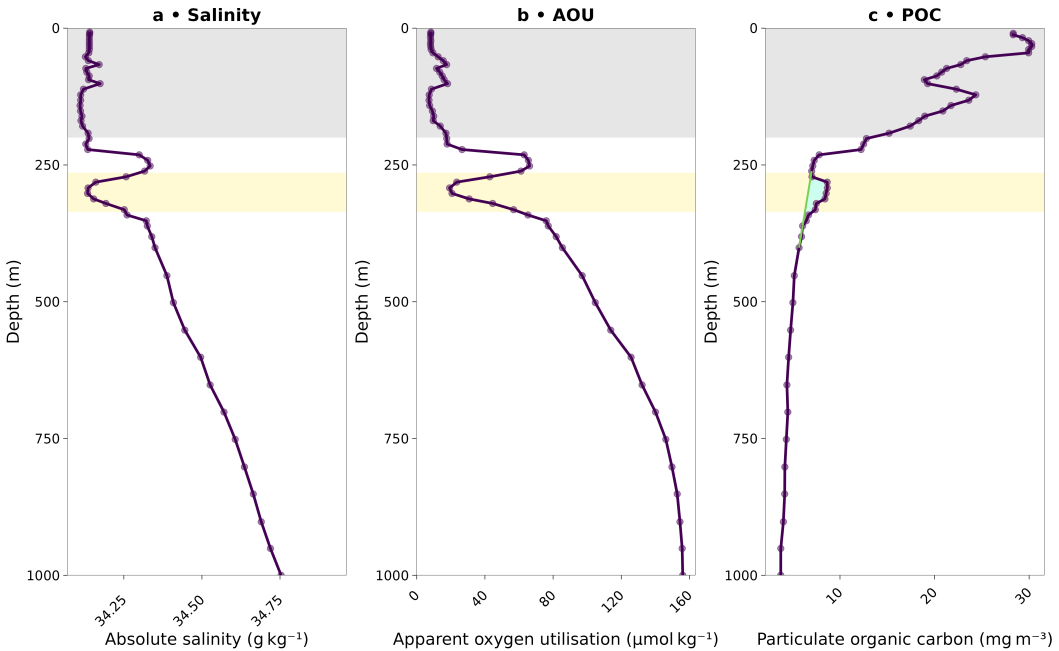


Figure 1. Vertical profiles from one Argo float in the Southern Ocean: (a) Salinity, (b) Apparent Oxygen Utilization (AOU) and (c) POC derived from backscatter propagation at 700 nanometers (Galí et al., 2022). Yellow shading shows the carbon subduction event detected by the algorithm using salinity, AOU and POC anomalies. Gray shading shows the top 200 meters of the water column skipped by the detection algorithm (no detection in top 200 m). Green line and light blue shading shows the depth-integrated POC anomaly ($\text{POC}_{\text{int}} = 121 \text{ mg/m}^2$ in this case). Data are from float WMO5904676 cycle 58 on October 5, 2017 at 49.3°S , 110°E .

the water column stratification (Kara et al., 2003; Sérazin et al., 2023) and a relative lack of phytoplankton blooms (Callies et al., 2016; Agarwal et al., 2024). In contrast, the spring peak in the North Atlantic and the Southern Ocean is consistent with Erickson and Thompson (2018), who found that eddy subduction in the Northeast Atlantic occurs over a narrow late winter to early spring window, when strong physical instabilities coincide with elevated surface carbon content. This result, however, challenges other work suggesting that carbon subduction observed in 7 Argo floats in the subpolar North Atlantic peaks in summer (A. R. Johnson & Omand, 2021). Surprisingly, the North Pacific shows no statistically significant seasonality, despite a noticeable, yet undersampled, spike in the Fall. Sparse Argo data likely mask any seasonality that might exist in the Kuroshio region or elsewhere in the subpolar Pacific.

4.3 Subduction hotspots found in high EKE regions

There is an ongoing discussion regarding the generating processes at play behind physical subduction events. Physical eddy subduction events are by-products of the re-stratification of submesoscale fronts (Taylor & Thompson, 2023; Lévy et al., 2024), but the mechanisms governing front formation and restratification of these fronts remain poorly understood and debated. As we mentioned in the introduction and results sections, fronts may emerge either because of spontaneous frontogenesis or forced frontogenesis (Blumen, 2000; Shakespeare & Taylor, 2013). Spontaneous frontogenesis is driven by inertial adjustment of an initially unbalanced flow and can develop in a matter of hours (Blumen,

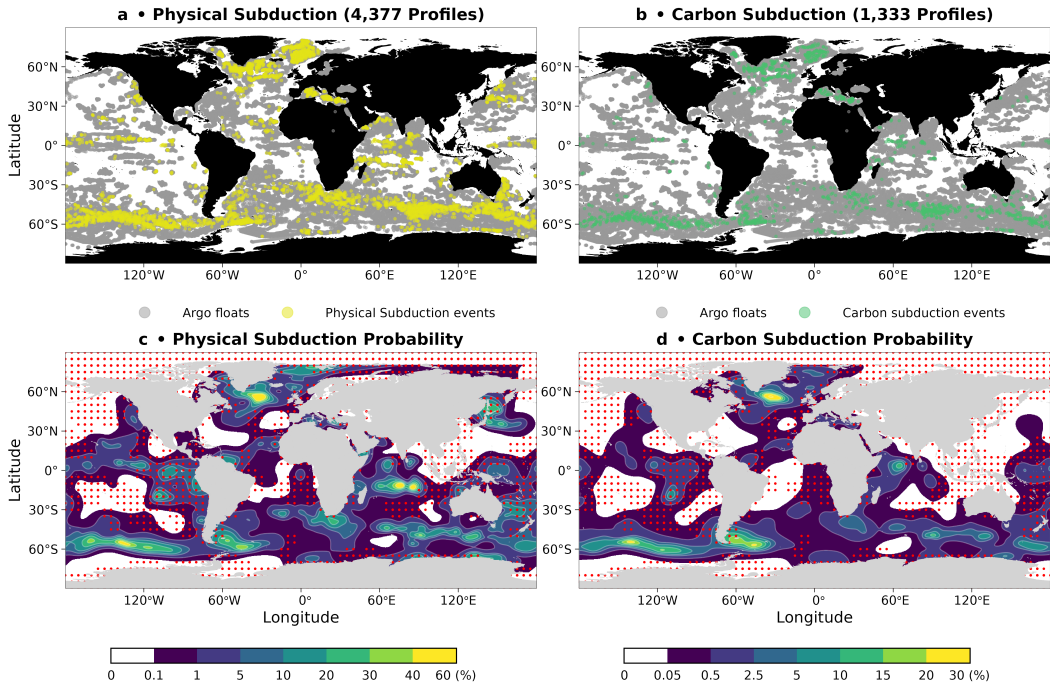


Figure 2. Spatial distribution of detected physical subduction events and carbon subduction events, raw observations and interpolated. (a) Argo profiles where physical subduction events were detected (yellow dots) and where no physical subduction events were detected (gray dots). (b) Argo profiles where carbon subduction events were detected (green dots) and where no physical subduction events were detected (gray dots). (c,d) Maps of probability that an Argo float detects a physical subduction event (c) and a carbon subduction event (d). Probabilities are estimated from generalized additive models (GAMs). Red stippling indicates 5 degree grid cells with no Argo profiles, indicating insufficient spatial coverage.

571 2000; Shakespeare & Taylor, 2013). In contrast, forced frontogenesis results from per-
 572 sistent mesoscale strain in regions of high balanced EKE and typically unfolds over days
 573 to weeks (Hoskins & Bretherton, 1972; Shakespeare & Taylor, 2013).

574 The positive association between hotspots of physical subduction and of balanced
 575 EKE in the extratropics is consistent with a slow, forced frontogenesis pathway: persis-
 576 tent mesoscale strain builds intense, long-lived fronts whose secondary circulations are
 577 strong enough to penetrate well beneath the export horizon. In contrast, balanced EKE
 578 is negatively correlated with subduction at tropical latitudes, suggesting that a faster,
 579 spontaneous adjustment energized by inertial oscillations, might dominate there. If in
 580 the tropics spontaneous frontogenesis dominates, its shorter time scale, on the order of
 581 hours (Shakespeare & Taylor, 2013), makes it extremely difficult to simulate in models
 582 and could partially explain why even high-resolution biogeochemical models show much
 583 weaker activity of the eddy subduction pump in the tropics than in the extratropics (Resplandy
 584 et al., 2019).

585 The consistent and robust negative association between unbalanced EKE and the
 586 probability of physical subduction in both the tropics and the extratropics might sug-
 587 gest that vigorous internal tides and internal gravity waves siphon energy away from the
 588 balanced mesoscale strain field, flattening fronts and suppressing both forced and spon-
 589 taneous frontogenesis (Shakespeare & Taylor, 2013; Thomas, 2017). This competition

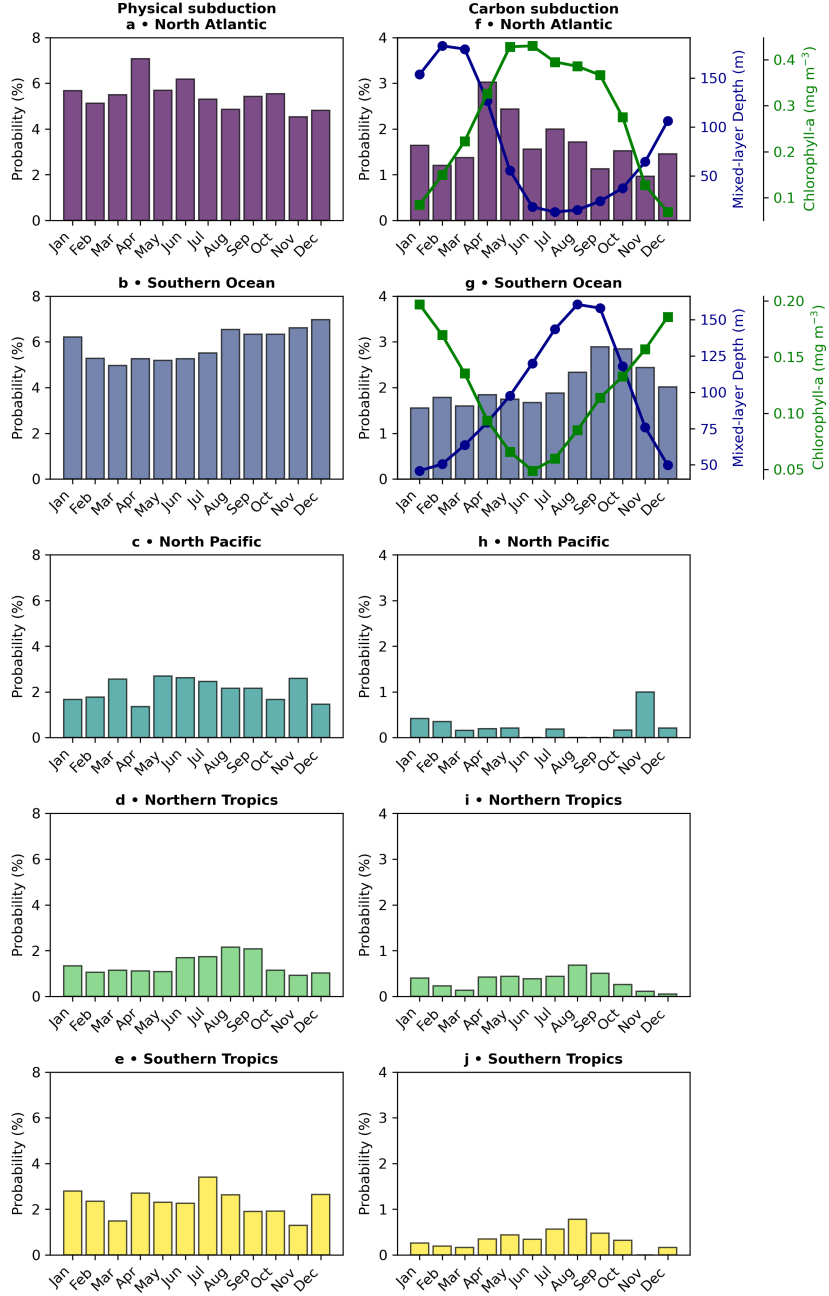


Figure 3. Monthly probability of carbon subduction and physical subduction event in five ocean regions. (a,f) North Atlantic ($\text{latitude} \geq 30^\circ\text{N}$). (b,g) Southern Ocean ($\text{latitude} \geq 30^\circ\text{S}$). (c,h) North Pacific ($\text{latitude} > 30^\circ\text{N}$). (d,i) Northern Tropics ($0^\circ < \text{latitude} < 30^\circ\text{N}$). (e,j) Southern Tropics ($0^\circ \leq \text{latitude} < 30^\circ\text{S}$). Regional monthly climatologies of chlorophyll from observation-based products (Melin, 2013) and mixed layer depth from biogeochemical Argo floats are overlaid on panels f and g. In the North Atlantic and Southern Ocean, carbon subduction exhibits significant seasonality, peaking after mixed layer depth reaches its maximum but before chlorophyll's monthly climatology peaks (a,c).

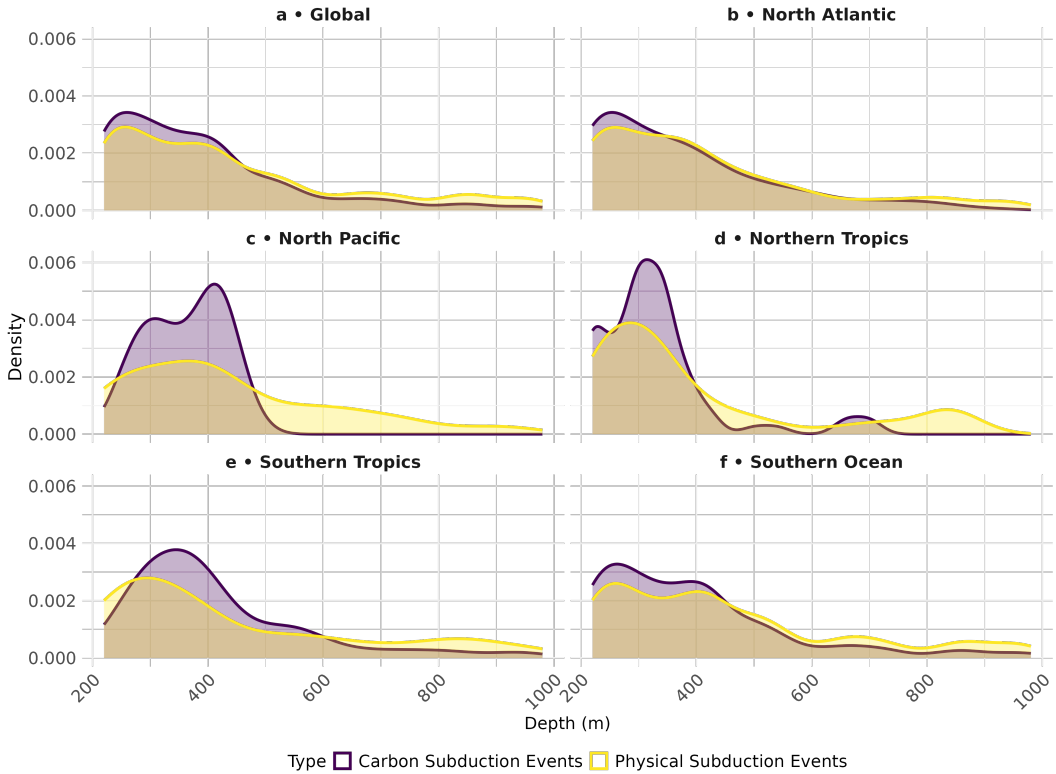


Figure 4. Depth of physical subduction events (yellow) and carbon subduction events (purple) for: (a) global ocean, (b) North Atlantic, (c) North Pacific, (d) Northern Tropics, (e) Southern Tropics, (f) Southern Ocean.

of internal tides and gravity waves with physical subduction could explain why fewer sustained subduction events are observed when unbalanced EKE is high.

4.4 Contributions from symmetric and mixed layer instabilities

The restratification of submesoscale fronts is due to physical instabilities such as symmetric instabilities (Thomas et al., 2013; Bachman et al., 2017) or mixed layer instabilities (Boccaletti et al., 2007; Fox-Kemper et al., 2008) or, most often, a conjunction of both (Stamper & Taylor, 2017). We present statistical evidence that the detected subduction events are associated with less stable and weakly stratified upper ocean conditions typical of symmetric instabilities (i.e. low Brunt-Väisälä frequency, N^2), more often than with deep mixed layers typical of mixed layer instabilities. This echoes earlier observational findings indicating that symmetric instabilities may rival or exceed the role of mixed layer instabilities in generating physical subduction (Erickson & Thompson, 2018; M. L. Chen & Schofield, 2024). This is further supported by modeling work: hotspots of physical subduction we identified in the Southern Ocean (e.g., Kerguelen Plateau, East-Pacific Antarctic Ridge, Drake Passage) overlap strikingly with regions of enhanced symmetric instability diagnosed in simulations by Dong et al. (2021), reinforcing the view that symmetric instabilities are an important driver of the eddy subduction pump.

These considerations are important because the type of instability driving physical and carbon subduction determines how the eddy subduction pump can be represented in biogeochemical models. mixed layer instabilities require a horizontal resolution of about

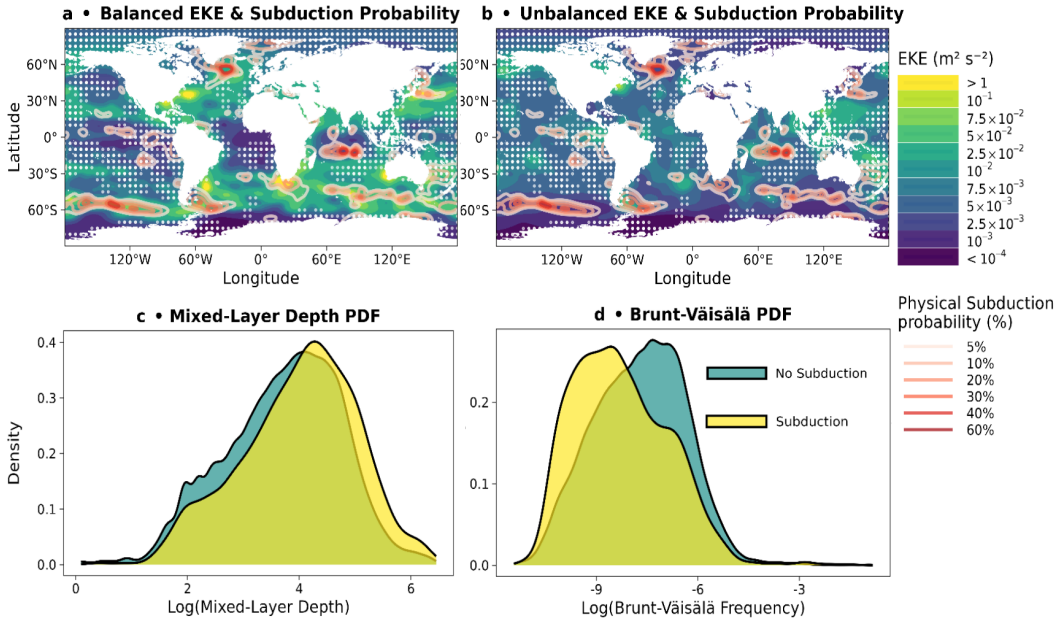


Figure 5. Physical drivers of subduction. (a,b) balanced and unbalanced eddy kinetic energy (EKE) from (Qiu et al., 2018), overlaid with contour lines (red) of the probability that an Argo float captures a physical subduction event. Stippling indicates 5-degree grid cells with no Argo profiles, indicating insufficient spatial coverage. (c,d) Probability density functions of mixed layer depth (c) and Brunt-Väisälä squared frequency (d) for profiles with physical subduction (yellow curve) and without physical subduction (teal curve). The lower overlap in Brunt-Väisälä squared frequency probability density functions suggests that Brunt-Väisälä squared frequency differences better predict subduction than mixed layer depth.

1 km (Boccaletti et al., 2007), whereas symmetric instabilities demand meter-scale resolution (Dong et al., 2021). Achieving a symmetric instabilities resolving, metric-scale resolution in global climate models may remain out of reach for another century, assuming the current exponential trend in model resolution improvement continues (Stamper & Taylor, 2017; Dong et al., 2021).

Our argument in favor of symmetric instabilities rather than mixed layer instabilities deserves scrutiny. Indeed, this argument is statistical rather than mechanistic, and both N^2 and MLD are estimated at the time of the subduction event's detection by the Argo float, rather than at the time the event occurred. The time lag between the subduction and the detection might be up to three months, especially in particularly quiet, low mean-flow and low EKE regions (e.g., Southern Rockall Trough) as it was shown by A. R. Johnson and Omand (2021). Therefore, the mixed layer depth and water column stratification at time of detection might be quite different from what they were at time of subduction. Additionally, the fact that we only look at subduction events beyond 200 meters might imply that we miss subduction events, as it was shown by Mahadevan et al. (2020) that subduction driven by mixed layer instabilities in the Mediterranean was very shallow, occurring in the top 150 meters of the ocean.

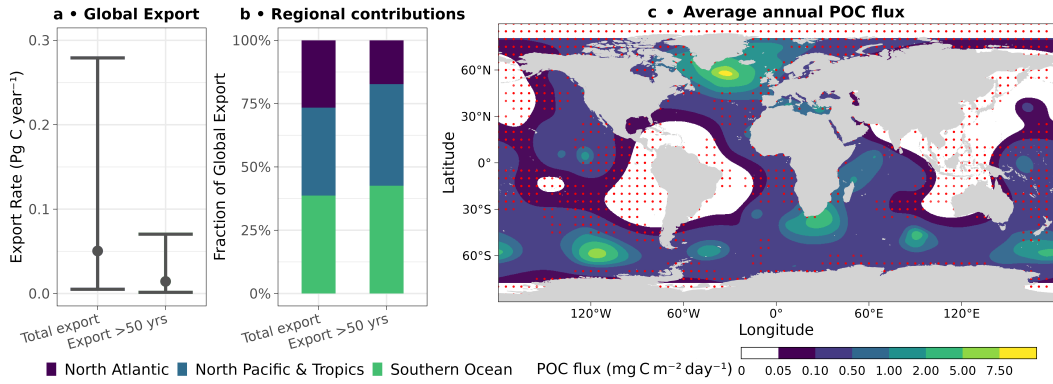


Figure 6. Global eddy subduction pump. (a) Global annual eddy subduction POC flux exported below 200 m: total flux (in blue) and flux exported in water masses that stay out of contact with the atmosphere for more than 50 years (in green). The central value corresponds to a subduction characteristic velocity of $W = 200 \text{ m d}^{-1}$, while the lower and upper end values correspond to $W = 20 \text{ m d}^{-1}$ and $W = 500 \text{ m d}^{-1}$. b) Regional relative contributions to annual eddy subduction POC flux: total and exported for more than 50 years. (c) Spatial distribution of total annual mean POC flux below 200 m assuming an average vertical velocity $W = 200 \text{ m day}^{-1}$. Red stippling marks 5° grid cells without Argo profiles (insufficient coverage). Turnover timescales are taken from dissolved inorganic carbon-based estimates in (Siegel et al., 2021).

627

4.5 Limitations

628
629
630
631
632
633
634
635
636
637
638
639
640

The main limitations hindering the investigation of the eddy subduction pump through Argo floats are the insufficient spatial and temporal coverage of the Argo database. The chronic undersampling of the Pacific Ocean, the Tropics, and the Arctic Ocean (see section 2.1) makes it hard to give any estimates of the magnitude and seasonality of the eddy pump in those regions. For instance, the absence of a seasonal carbon subduction hotspot in the Kuroshio came as a surprise. However, it is hard to determine whether this absence is due to a generally lower biological productivity of the North-Western Pacific Ocean relative to the North Atlantic, as was shown by Lee et al. (1981); Kimura et al. (1997); Kasai et al. (2002) or insufficient coverage of the region by Argo floats (see Figure S1 in SI). On the other hand, the particularly well-sampled hotspot downstream of the Kerguelen may have led Llort et al. (2018) to overestimate the importance of this hotspot of carbon subduction relative to other hotspots in the Southern Ocean, near the East-Pacific Antarctic Ridge or downstream of the Drake passage.

641
642
643
644
645
646
647
648
649
650
651

An additional limitation is the lack of information on vertical velocities of carbon subduction and the age of carbon subduction which are required to infer the eddy subduction POC export flux. In this study we used a range of characteristic subduction velocities, $W \in [20, 500] \text{ m d}^{-1}$, and apply it uniformly to all detected events. Because the local daily export flux (Q) scales linearly with the vertical velocity (W), see equation (3), the one order of magnitude spread in the vertical velocity propagates directly into an order of magnitude uncertainty in our global export estimate. Ideally, one would estimate a velocity specific to each individual filament, but such information cannot be recovered from Argo profiles alone. Furthermore, by fixing a global export horizon of 200 meters, we may have missed superficial carbon subduction events confined to the mixed layer, as is the case for the Mediterranean Sea (Mahadevan et al., 2020).

Event age adds further uncertainty. The POC anomaly observed by a float is only the residue of the original export, remineralization and lateral diffusion erode the signal between subduction and detection by the Argo float. We correct for this loss by assuming a maximum lag of three months and an e-folding decay time of 90 days, following A. R. Johnson and Omand (2021). While appropriate for relatively quiescent basins, this correction is likely conservative in energetic regions such as the Antarctic Circumpolar Current, where coherent POC anomalies dissipate more rapidly. In such settings a larger multiplicative factor would be required to recover the initial export. Taken together, the uncertainties in both the timing of observation and the choice of W expand the plausible range of the eddy-subduction export by roughly two orders of magnitude.

In addition, Argo floats are unable to measure dissolved organic carbon (DOC), effectively only measuring a fraction of the downward flux of carbon. Eddy-driven subduction has been recognized to export DOC along with POC (Omand et al., 2015; Resplandy et al., 2019), and may even be exporting nearly as much DOC as POC (55% of POC and 45 % of DOC) (Resplandy et al., 2019; Poupon et al., 2025). Argo floats are unable to measure DOC and therefore provide an incomplete view of carbon export by the eddy subduction pump. Moreover, Argo floats do not detect upward fluxes of organic carbon that could partially offset the contribution of carbon subduction events to the eddy subduction pump (Resplandy et al., 2019). In fact, all exports reported here are gross downward fluxes. We do not quantify compensating upwards fluxes, and therefore we do not interpret the export fluxes estimates as net carbon sequestration or as an offset of anthropogenic emissions.

4.6 Implications for the Global Biological Carbon Pump

Our global estimate of the annual export flux of POC by the eddy subduction pump is $0.05 [<0.01\text{---}0.28] \text{ Pg C yr}^{-1}$. This estimate sits at the low end of the $0\text{--}2 \text{ Pg C yr}^{-1}$ global estimate of (Boyd et al., 2019), based on extrapolations of Llort et al. (2018)'s Southern Ocean study to the globe. Our estimate of the magnitude of the eddy subduction pump represents less than 5% of the total export of POC by the biological pump ($\sim 10 \text{ Pg C yr}^{-1}$; Boyd et al. (2019); Nowicki et al. (2022); Wang et al. (2023)). Incorporating dissolved organic carbon using the $\sim 55\%$ POC / 45% DOC partitioning from (Poupon et al., 2025) would raise our estimate to $0.10 [<0.01\text{---}0.51] \text{ Pg C yr}^{-1}$. Even then, the eddy subduction pump still represents less than 5 % of the total export of organic carbon, which is $\sim 12 \text{ Pg C yr}^{-1}$ including POC and DOC (Boyd et al., 2019), which is consistent with (Resplandy et al., 2019). Moreover, we estimate that only 25% of exported POC enters waters with reemergence times larger than 50 years, consistent with rapid remineralization of physically exported POC found by Poupon et al. (2025). Overall, the relatively small contribution of the eddy subduction pump suggests that it can likely be neglected for first-order estimates of the total biological carbon export. This is good news, given that current climate models lack the resolution to capture the effects of the eddy subduction pump on the global carbon budget.

5 Conclusion

We present a framework for the global detection of the eddy subduction pump, finding springtime hotspots in the Southern Ocean and the North Atlantic associated with high eddy kinetic energy. We estimated the POC export flux attributable to the eddy subduction pump to $0.05 \text{ Pg C yr}^{-1}$ with a likely range ($<0.01\text{---}0.28 \text{ Pg C yr}^{-1}$). This estimate may be updated when more Argo float data becomes available. We present some evidence that the eddy subduction pump is due to an interplay of mixed layer and symmetric instabilities, which are processes that happen at scales which are beyond the reach of global biogeochemical ocean models and Earth system models. However, the small magnitude of the export rate of the subduction pump, less than 5% of the total export of

702 particulate organic carbon by the biological pump, seem to suggest that the adequate
 703 representation of the eddy subduction pump in ocean models is not a priority for reducing
 704 our uncertainty on the global ocean carbon budget.

705 Open Research Section

706 Float data were downloaded from the USGODAE archive; <https://argo.ucsd.edu/data/data-from-gdacs/> using the OneArgo-R toolbox <https://github.com/NOAA-PMEL/OneArgo-R> (Cornec et al., 2022), developed by NOAA-PMEL and licensed under GNU
 707 General Public License v3.0 (GPL-3, 29 June 2007). Our analysis used delayed-mode,
 708 quality-controlled data retrieved on 6 May 2024.

709 All analyses were conducted in R (version 4.4.1; released 14 June 2024), which is
 710 distributed under GNU GPL v3, with the tidyverse suite used for data manipulation and
 711 visualization (Wickham et al., 2019). Statistical modeling and generalized additive mod-
 712 els (GAMs) fittings employed the mgcv package (Wood, 2017). Thermodynamic vari-
 713 ables were computed using TEOS-10 implementations in the gsw package (McDougall
 714 & Barker, 2011; Kelley et al., 2024). The code associated with this manuscript for data
 715 processing and analysis, including an implementation of the detection algorithm in R is
 716 licensed under GNU GPL v3 and published on Zenodo (Keutgen, 2025).

719 Conflict of Interests Statement

720 The authors have no conflicts of interest to declare that are relevant to the con-
 721 tent of this article.

722 Acknowledgments

723 The authors are grateful to Stephan A. Fueglisterler for his comments regarding the meth-
 724 ods section. The authors gratefully acknowledge the NSF-Chemical Oceanography award
 725 2023108 on the Eddy Effects on the Biological Carbon Pump. The authors are grate-
 726 ful to the international Biogeochemical-Argo program, which is developing a global net-
 727 work of profiling floats with biogeochemical sensors.

728 References

- 729 Agarwal, V., Chávez-Casillas, J., Inomura, K., & Mouw, C. B. (2024, Febru-
 730 ary). Patterns in the temporal complexity of global chlorophyll concentra-
 731 tion. *Nature Communications*, 15(1), 1522. Retrieved 2025-04-24, from
 732 <https://www.nature.com/articles/s41467-024-45976-8> (Publisher:
 733 Nature Publishing Group) doi: 10.1038/s41467-024-45976-8
- 734 Bachman, S. D., Fox-Kemper, B., Taylor, J. R., & Thomas, L. N. (2017, January).
 735 Parameterization of Frontal Symmetric Instabilities. I: Theory for Resolved
 736 Fronts. *Ocean Modelling*, 109, 72–95. Retrieved 2024-03-20, from <https://www.sciencedirect.com/science/article/pii/S1463500316301482> doi:
 737 10.1016/j.ocemod.2016.12.003
- 738 Bittig, H. C., Maurer, T. L., Plant, J. N., Schmechtig, C., Wong, A. P. S., Claus-
 739 tre, H., ... Xing, X. (2019, August). A BGC-Argo Guide: Planning, De-
 740 ployment, Data Handling and Usage. *Frontiers in Marine Science*, 6. Re-
 741 trieved 2024-05-06, from <https://www.frontiersin.org/articles/10.3389/fmars.2019.00502> (Publisher: Frontiers) doi: 10.3389/fmars.2019.00502
- 742 Blumen, W. (2000, January). Inertial Oscillations and Frontogenesis in a Zero
 743 Potential Vorticity Model. *Journal of Physical Oceanography*. Retrieved
 744 2024-06-30, from https://journals.ametsoc.org/view/journals/phoc/30/1/1520-0485_2000_030_0031_ioafia_2.0.co_2.xml (Section: Journal of

- Physical Oceanography)
- Boccaletti, G., Ferrari, R., & Fox-Kemper, B. (2007, September). Mixed Layer Instabilities and Restratification. *Journal of Physical Oceanography*, 37(9), 2228–2250. Retrieved 2024-03-27, from <https://journals.ametsoc.org/view/journals/phoc/37/9/jpo3101.1.xml> (Publisher: American Meteorological Society Section: Journal of Physical Oceanography) doi: 10.1175/JPO3101.1
- Boyd, P. W., Claustre, H., Levy, M., Siegel, D. A., & Weber, T. (2019, April). Multi-faceted particle pumps drive carbon sequestration in the ocean. *Nature*, 568(7752), 327–335. Retrieved 2023-05-19, from <https://www.nature.com/articles/s41586-019-1098-2> (Number: 7752 Publisher: Nature Publishing Group) doi: 10.1038/s41586-019-1098-2
- Callies, J., Flierl, G., Ferrari, R., & Fox-Kemper, B. (2016, February). The role of mixed-layer instabilities in submesoscale turbulence. *Journal of Fluid Mechanics*, 788, 5–41. Retrieved 2024-05-28, from <https://www.cambridge.org/core/journals/journal-of-fluid-mechanics/article/role-of-mixedlayer-instabilities-in-submesoscale-turbulence/8B7EE19309A6442EDEDEAEABC61E05F4> doi: 10.1017/jfm.2015.700
- Chen, M. L., & Schofield, O. (2024). Spatial and Seasonal Controls on Eddy Subduction in the Southern Ocean. *Geophysical Research Letters*, 51(20), e2024GL109246. Retrieved 2024-11-15, from <https://onlinelibrary.wiley.com/doi/abs/10.1029/2024GL109246> (eprint: <https://onlinelibrary.wiley.com/doi/pdf/10.1029/2024GL109246>) doi: 10.1029/2024GL109246
- Chen, S., Wells, M. L., Huang, R. X., Xue, H., Xi, J., & Chai, F. (2021, October). Episodic subduction patches in the western North Pacific identified from BGC-Argo float data. *Biogeosciences*, 18(19), 5539–5554. Retrieved 2023-11-06, from <https://bg.copernicus.org/articles/18/5539/2021/> (Publisher: Copernicus GmbH) doi: 10.5194/bg-18-5539-2021
- Cornec, M., Huang, Y., Jutard, Q., Sauzède, R., & Schmechtig, C. (2022, June). *OneArgo-R: An R toolbox for accessing and visualizing Argo data*. Zenodo. Retrieved 2024-05-07, from <https://zenodo.org/records/6604651> doi: 10.5281/zenodo.6604651
- de Boyer Montégut, C., Madec, G., Fischer, A. S., Lazar, A., & Iudicone, D. (2004). Mixed layer depth over the global ocean: An examination of profile data and a profile-based climatology. *Journal of Geophysical Research: Oceans*, 109(C12). Retrieved 2024-11-11, from <https://onlinelibrary.wiley.com/doi/abs/10.1029/2004JC002378> (eprint: <https://onlinelibrary.wiley.com/doi/pdf/10.1029/2004JC002378>) doi: 10.1029/2004JC002378
- DeVries, T. (2022, October). The Ocean Carbon Cycle. *Annual Review of Environment and Resources*, 47(Volume 47, 2022), 317–341. Retrieved 2024-04-04, from <https://www.annualreviews.org/content/journals/10.1146/annurev-environ-120920-111307> (Publisher: Annual Reviews) doi: 10.1146/annurev-environ-120920-111307
- Dong, J., Fox-Kemper, B., Zhang, H., & Dong, C. (2021, May). The Scale and Activity of Symmetric Instability Estimated from a Global Submesoscale-Permitting Ocean Model. *Journal of Physical Oceanography*, 51(5), 1655–1670. Retrieved 2024-03-27, from <https://journals.ametsoc.org/view/journals/phoc/51/5/JPO-D-20-0159.1.xml> (Publisher: American Meteorological Society Section: Journal of Physical Oceanography) doi: 10.1175/JPO-D-20-0159.1
- Erickson, Z. K., & Thompson, A. F. (2018). The Seasonality of Physically Driven Export at Submesoscales in the Northeast Atlantic Ocean. *Global Biogeochemical Cycles*, 32(8), 1144–1162. Retrieved 2023-11-28, from <https://onlinelibrary.wiley.com/doi/abs/10.1029/2018GB005927>

- ([_eprint](https://onlinelibrary.wiley.com/doi/pdf/10.1029/2018GB005927): <https://onlinelibrary.wiley.com/doi/pdf/10.1029/2018GB005927>)
doi: 10.1029/2018GB005927

Falkowski, P. G., Barber, R. T., & Smetacek, V. (1998, July). Biogeochemical Controls and Feedbacks on Ocean Primary Production. *Science*, 281(5374), 200–206. Retrieved 2024-05-06, from <https://www.science.org/doi/full/10.1126/science.281.5374.200> (Publisher: American Association for the Advancement of Science) doi: 10.1126/science.281.5374.200

Fox-Kemper, B., Ferrari, R., & Hallberg, R. (2008, June). Parameterization of Mixed Layer Eddies. Part I: Theory and Diagnosis. *Journal of Physical Oceanography*, 38(6), 1145–1165. Retrieved 2024-03-20, from <https://journals.ametsoc.org/view/journals/phoc/38/6/2007jpo3792.1.xml> (Publisher: American Meteorological Society Section: Journal of Physical Oceanography) doi: 10.1175/2007JPO3792.1

Frenger, I., Landolfi, A., Kvale, K., Somes, C. J., Oschlies, A., Yao, W., & Koeve, W. (2024). Misconceptions of the marine biological carbon pump in a changing climate: Thinking outside the “export” box. *Global Change Biology*, 30(1), e17124. Retrieved 2025-01-30, from <https://onlinelibrary.wiley.com/doi/abs/10.1111/gcb.17124> doi: 10.1111/gcb.17124

Galí, M., Falls, M., Claustre, H., Aumont, O., & Bernardello, R. (2022, March). Bridging the gaps between particulate backscattering measurements and modeled particulate organic carbon in the ocean. *Biogeosciences*, 19(4), 1245–1275. Retrieved 2025-04-11, from <https://bg.copernicus.org/articles/19/1245/2022/> (Publisher: Copernicus GmbH) doi: 10.5194/bg-19-1245-2022

Hastie, T., Friedman, J., & Tibshirani, R. (2001). *The Elements of Statistical Learning*. New York, NY: Springer. Retrieved 2023-08-18, from <http://link.springer.com/10.1007/978-0-387-21606-5> doi: 10.1007/978-0-387-21606-5

Hastie, T., & Tibshirani, R. (1986, August). Generalized Additive Models. *Statistical Science*, 1(3), 297–310. Retrieved 2025-08-25, from <https://projecteuclid.org/journals/statistical-science/volume-1/issue-3/Generalized-Additive-Models/10.1214/ss/1177013604.full> (Publisher: Institute of Mathematical Statistics) doi: 10.1214/ss/1177013604

Hoskins, B. J., & Bretherton. (1972). *Atmospheric Frontogenesis Models: Mathematical Formulation and Solution* in: *Journal of the Atmospheric Sciences Volume 29 Issue 1 (1972)*. Retrieved 2024-06-30, from https://journals.ametsoc.org/view/journals/atsc/29/1/1520-0469_1972_029_0011_afmmfa_2_0_co_2.xml?tab_body=pdf

Huber, P. J. (2004). *Robust Statistics*. John Wiley & Sons. (Google-Books-ID: e62RhdqIdMkC)

Johnson, A. R., & Omand, M. M. (2021). Evolution of a Subducted Carbon-Rich Filament on the Edge of the North Atlantic Gyre. *Journal of Geophysical Research: Oceans*, 126(2), e2020JC016685. Retrieved 2023-10-30, from <https://onlinelibrary.wiley.com/doi/abs/10.1029/2020JC016685> ([_eprint](https://onlinelibrary.wiley.com/doi/pdf/10.1029/2020JC016685): <https://onlinelibrary.wiley.com/doi/pdf/10.1029/2020JC016685>) doi: 10.1029/2020JC016685

Johnson, K. S., Plant, J. N., Coletti, L. J., Jannasch, H. W., Sakamoto, C. M., Riser, S. C., ... Sarmiento, J. L. (2017). Biogeochemical sensor performance in the SOCCOM profiling float array. *Journal of Geophysical Research: Oceans*, 122(8), 6416–6436. Retrieved 2024-05-13, from <https://onlinelibrary.wiley.com/doi/abs/10.1002/2017JC012838> ([_eprint](https://onlinelibrary.wiley.com/doi/pdf/10.1002/2017JC012838): <https://onlinelibrary.wiley.com/doi/pdf/10.1002/2017JC012838>) doi: 10.1002/2017JC012838

Kara, A. B., Rochford, P. A., & Hurlburt, H. E. (2003). Mixed layer depth variability over the global ocean. *Journal of Geophysical Research: Oceans*, 108(C3). Retrieved 2025-07-08, from <https://onlinelibrary.wiley.com/doi/abs/10.1029/2003JC012838>

- onlinelibrary.wiley.com/doi/abs/10.1029/2000JC000736 (*eprint*: https://agupubs.onlinelibrary.wiley.com/doi/pdf/10.1029/2000JC000736) doi: 10.1029/2000JC000736

Kasai, A., Kimura, S., Nakata, H., & Okazaki, Y. (2002, November). Entrainment of coastal water into a frontal eddy of the Kuroshio and its biological significance. *Journal of Marine Systems*, 37(1), 185–198. Retrieved 2025-06-18, from https://www.sciencedirect.com/science/article/pii/S0924796302002014 doi: 10.1016/S0924-7963(02)00201-4

Kelley, D., Richards, C., & SCOR/IAPSO, W. (2024). *gsw: Gibbs Sea Water Functions*. Retrieved from https://CRAN.R-project.org/package=gsw

Keutgen, M. (2025, September). *mkeutgen/globargo: v.0.1-alpha*. Zenodo. Retrieved 2025-09-30, from https://zenodo.org/records/17236581 doi: 10.5281/zenodo.17236581

Kimura, S., Kasai, A., Nakata, H., Sugimoto, T., Simpson, J. H., & Cheok, J. V. S. (1997, April). Biological productivity of meso-scale eddies caused by frontal disturbances in the Kuroshio. *ICES Journal of Marine Science*, 54(2), 179–192. Retrieved 2025-06-18, from https://doi.org/10.1006/jmsc.1996.0209 doi: 10.1006/jmsc.1996.0209

Lacour, L., Briggs, N., Claustre, H., Ardyna, M., & Dall'Olmo, G. (2019). The Intraseasonal Dynamics of the Mixed Layer Pump in the Subpolar North Atlantic Ocean: A Biogeochemical-Argo Float Approach. *Global Biogeochemical Cycles*, 33(3), 266–281. Retrieved 2024-10-15, from https://onlinelibrary.wiley.com/doi/abs/10.1029/2018GB005997 (*eprint*: https://onlinelibrary.wiley.com/doi/pdf/10.1029/2018GB005997) doi: 10.1029/2018GB005997

Lacour, L., Llort, J., Briggs, N., Strutton, P. G., & Boyd, P. W. (2023, March). Seasonality of downward carbon export in the Pacific Southern Ocean revealed by multi-year robotic observations. *Nature Communications*, 14(1), 1278. Retrieved 2023-05-21, from https://www.nature.com/articles/s41467-023-36954-7 (Number: 1 Publisher: Nature Publishing Group) doi: 10.1038/s41467-023-36954-7

Lee, T. N., Atkinson, L. P., & Legeckis, R. (1981, April). Observations of a Gulf Stream frontal eddy on the Georgia continental shelf, April 1977. *Deep Sea Research Part A. Oceanographic Research Papers*, 28(4), 347–378. Retrieved 2025-06-18, from https://www.sciencedirect.com/science/article/pii/0198014981900042 doi: 10.1016/0198-0149(81)90004-2

Llort, J., Langlais, C., Matear, R., Moreau, S., Lenton, A., & Strutton, P. G. (2018). Evaluating Southern Ocean Carbon Eddy-Pump From Biogeochemical-Argo Floats. *Journal of Geophysical Research: Oceans*, 123(2), 971–984. Retrieved 2023-05-21, from https://onlinelibrary.wiley.com/doi/abs/10.1002/2017JC012861 (*eprint*: https://onlinelibrary.wiley.com/doi/pdf/10.1002/2017JC012861) doi: 10.1002/2017JC012861

Lévy, M., Couespel, D., Haëck, C., Keerthi, M., Mangolte, I., & Prend, C. J. (2024). The Impact of Fine-Scale Currents on Biogeochemical Cycles in a Changing Ocean. *Annual Review of Marine Science*, 16(1), null. Retrieved 2023-10-16, from https://doi.org/10.1146/annurev-marine-020723-020531 (*eprint*: https://doi.org/10.1146/annurev-marine-020723-020531) doi: 10.1146/annurev-marine-020723-020531

Mahadevan, A., Pascual, A., Rudnick, D. L., Ruiz, S., Tintoré, J., & D'Asaro, E. (2020, November). Coherent Pathways for Vertical Transport from the Surface Ocean to Interior. *Bulletin of the American Meteorological Society*, 101(11), E1996–E2004. Retrieved 2025-06-18, from https://journals.ametsoc.org/view/journals/bams/101/11/bamsD190305.xml (Publisher: American Meteorological Society Section: Bulletin of the American Meteorological Society)

- 913 doi: 10.1175/BAMS-D-19-0305.1
- 914 McDougall, T. J., & Barker, P. M. (2011). Getting started with TEOS-10 and the
915 Gibbs Seawater (GSW) oceanographic toolbox. *Scor/iapso WG*, 127(532), 1–
916 28. Retrieved 2024-05-07, from http://www.teos-10.org/pubs/gsw/v3_04/pdf/Getting Started.pdf
- 917 McDougall, T. J., Barker, P. M., & Stanley, G. J. (2021). Spice Variables
918 and Their Use in Physical Oceanography. *Journal of Geophysical Research: Oceans*, 126(2), e2019JC015936.
919 Retrieved 2024-04-02, from <https://onlinelibrary.wiley.com/doi/abs/10.1029/2019JC015936>
920 (_eprint: <https://onlinelibrary.wiley.com/doi/pdf/10.1029/2019JC015936>)
921 doi: 10.1029/2019JC015936
- 922 McDougall, T. J., & Krzysik, O. A. (2015). Spiciness. *Journal of Marine Research*,
923 73(5), 141–152. Retrieved 2024-05-22, from <https://www.ingentaconnect.com/contentone/jmr/jmr/2015/00000073/00000005/art00002> (Publisher:
924 Sears Foundation for Marine Research)
- 925 Melin, F. (2013, August). *EMIS - SeaWiFS Monthly climatology sea surface diffuse
926 attenuation coefficient at 490nm (4km) in m^-1*. Retrieved 2025-06-11, from
927 <http://data.europa.eu/89h/094dd2fb-7da0-45c9-826e-e9abf5181b3e>
(Publisher: European Commission, Joint Research Centre (JRC))
- 928 Nowicki, M., DeVries, T., & Siegel, D. A. (2022). Quantifying the Carbon Ex-
929 port and Sequestration Pathways of the Ocean's Biological Carbon Pump.
930 *Global Biogeochemical Cycles*, 36(3), e2021GB007083. Retrieved 2024-05-04,
931 from <https://onlinelibrary.wiley.com/doi/abs/10.1029/2021GB007083>
932 (_eprint: <https://onlinelibrary.wiley.com/doi/pdf/10.1029/2021GB007083>) doi:
933 10.1029/2021GB007083
- 934 Omand, M. M., D'Asaro, E. A., Lee, C. M., Perry, M. J., Briggs, N., Cetinić, I., &
935 Mahadevan, A. (2015, April). Eddy-driven subduction exports particulate
936 organic carbon from the spring bloom. *Science*, 348(6231), 222–225. Retrieved
937 2023-05-21, from <https://www.science.org/doi/10.1126/science.1260062>
(Publisher: American Association for the Advancement of Science) doi:
938 10.1126/science.1260062
- 939 Poupon, M., Resplandy, L., & Luo, J. (2025, May). *Unifying framework reveals im-
940 portance of dissolved fluxes in ocean biological carbon pump*. Research Square.
941 Retrieved 2025-06-28, from <https://www.researchsquare.com/article/rs-6666218/v1> (ISSN: 2693-5015) doi: 10.21203/rs.3.rs-6666218/v1
- 942 Qiu, B., Chen, S., Klein, P., Wang, J., Torres, H., Fu, L.-L., & Menemenlis, D.
943 (2018, March). Seasonality in Transition Scale from Balanced to Unbal-
944 anced Motions in the World Ocean. *Journal of Physical Oceanography*, 48(3),
945 591–605. Retrieved 2025-01-24, from <https://journals.ametsoc.org/view/journals/phoc/48/3/jpo-d-17-0169.1.xml>
946 (_eprint: <https://journals.ametsoc.org/doi/pdf/10.1175/JPO-D-17-0169.1>) doi:
947 10.1175/JPO-D-17-0169.1
- 948 Resplandy, L., Lévy, M., & McGillicuddy Jr., D. J. (2019). Effects of Eddy-
949 Driven Subduction on Ocean Biological Carbon Pump. *Global Biogeo-
950 chemical Cycles*, 33(8), 1071–1084. Retrieved 2023-06-24, from <https://onlinelibrary.wiley.com/doi/abs/10.1029/2018GB006125>
951 (_eprint: <https://onlinelibrary.wiley.com/doi/pdf/10.1029/2018GB006125>) doi:
952 10.1029/2018GB006125
- 953 Rousseeuw, P. J., & Hubert, M. (2018). Anomaly detection by robust statis-
954 tics. *WIREs Data Mining and Knowledge Discovery*, 8(2), e1236. Retrieved
955 2023-10-03, from <https://onlinelibrary.wiley.com/doi/abs/10.1002/widm.1236> doi: 10.1002/widm.1236
- 956 Shakespeare, C. J., & Taylor, J. R. (2013, December). A generalized mathemat-
957 ical model of geostrophic adjustment and frontogenesis: uniform potential
958 vorticity. *Journal of Fluid Mechanics*, 736, 366–413. Retrieved 2024-06-
959

- 968 25, from <https://www.cambridge.org/core/journals/journal-of-fluid-mechanics/article/generalized-mathematical-model-of-geostrophic-adjustment-and-frontogenesis-uniform-potential-vorticity/809C48C22ED63CE88E1CCAF715D22343> doi: 10.1017/jfm.2013.526
- 969
970
971
972 Siegel, D. A., DeVries, T., Cetinić, I., & Bisson, K. M. (2023, January). Quantifying
973 the Ocean's Biological Pump and Its Carbon Cycle Impacts on Global Scales.
974 *Annual Review of Marine Science*, 15(Volume 15, 2023), 329–356. Retrieved
975 2024-07-19, from <https://www.annualreviews.org/content/journals/10.1146/annurev-marine-040722-115226> (Publisher: Annual Reviews) doi:
976 10.1146/annurev-marine-040722-115226
- 977
978 Siegel, D. A., DeVries, T., Doney, S. C., & Bell, T. (2021, September). Assessing the
979 sequestration time scales of some ocean-based carbon dioxide reduction strate-
980 gies. *Environmental Research Letters*, 16(10), 104003. Retrieved 2025-03-26,
981 from <https://dx.doi.org/10.1088/1748-9326/ac0be0> (Publisher: IOP
982 Publishing) doi: 10.1088/1748-9326/ac0be0
- 983 Stamper, M. A., & Taylor, J. R. (2017, January). The transition from symmetric to
984 baroclinic instability in the Eady model. *Ocean Dynamics*, 67(1), 65–80. Re-
985 tried 2024-03-28, from <https://doi.org/10.1007/s10236-016-1011-6> doi:
986 10.1007/s10236-016-1011-6
- 987 Stukel, M. R., Aluwihare, L. I., Barbeau, K. A., Chekalyuk, A. M., Goericke, R.,
988 Miller, A. J., ... Landry, M. R. (2017, February). Mesoscale ocean fronts en-
989 hance carbon export due to gravitational sinking and subduction. *Proceedings
990 of the National Academy of Sciences*, 114(6), 1252–1257. Retrieved 2023-
991 11-28, from <https://www.pnas.org/doi/abs/10.1073/pnas.1609435114>
992 (Publisher: Proceedings of the National Academy of Sciences) doi:
993 10.1073/pnas.1609435114
- 994 Stukel, M. R., Song, H., Goericke, R., & Miller, A. J. (2018). The role of sub-
995 duction and gravitational sinking in particle export, carbon sequestration,
996 and the remineralization length scale in the California Current Ecosys-
997 tem. *Limnology and Oceanography*, 63(1), 363–383. Retrieved 2023-11-28,
998 from <https://onlinelibrary.wiley.com/doi/abs/10.1002/lno.10636>
999 (_eprint: <https://onlinelibrary.wiley.com/doi/pdf/10.1002/lno.10636>) doi:
1000 10.1002/lno.10636
- 1001 Sérazin, G., Trégouier, A. M., & de Boyer Montégut, C. (2023, March). A seasonal
1002 climatology of the upper ocean pycnocline. *Frontiers in Marine Science*,
1003 10. Retrieved 2025-07-08, from <https://www.frontiersin.org/journals/marine-science/articles/10.3389/fmars.2023.1120112/full> (Publisher:
1004 Frontiers) doi: 10.3389/fmars.2023.1120112
- 1005 Tailleux, R. (2021, January). Spiciness theory revisited, with new views on neutral
1006 density, orthogonality, and passiveness. *Ocean Science*, 17(1), 203–219. Re-
1007 tried 2024-04-02, from <https://os.copernicus.org/articles/17/203/2021/>
1008 (Publisher: Copernicus GmbH) doi: 10.5194/os-17-203-2021
- 1009 Taylor, J. R., & Thompson, A. F. (2023, January). Submesoscale Dynamics in the
1010 Upper Ocean. *Annual Review of Fluid Mechanics*, 55(Volume 55, 2023), 103–
1011 127. Retrieved 2024-03-19, from <https://www.annualreviews.org/content/journals/10.1146/annurev-fluid-031422-095147> (Publisher: Annual Re-
1012 views) doi: 10.1146/annurev-fluid-031422-095147
- 1013 Thomas, L. N. (2017, October). On the modifications of near-inertial waves
1014 at fronts: implications for energy transfer across scales. *Ocean Dynamics*,
1015 67(10), 1335–1350. Retrieved 2025-07-09, from <https://doi.org/10.1007/s10236-017-1088-6> doi: 10.1007/s10236-017-1088-6
- 1016 Thomas, L. N., Taylor, J. R., Ferrari, R., & Joyce, T. M. (2013, July). Sym-
1017 metric instability in the Gulf Stream. *Deep Sea Research Part II: Topical
1018 Studies in Oceanography*, 91, 96–110. Retrieved 2024-03-28, from <https://www.sciencedirect.com/science/article/pii/S0967064513000829> doi:
1019 10.1016/j.dsr2.2013.05.003
- 1020
1021
1022

- 1023 10.1016/j.dsr2.2013.02.025
 1024 Torres, H. S., Rodriguez, E., Wineteer, A., Klein, P., Thompson, A. F., Cal-
 1025 lies, J., ... Akbar, R. (2024, December). Airborne observations of fast-
 1026 evolving ocean submesoscale turbulence. *Communications Earth & Envi-
 1027 ronment*, 5(1), 771. Retrieved 2025-07-02, from <https://www.nature.com/articles/s43247-024-01917-3> (Publisher: Nature Publishing Group) doi:
 1029 10.1038/s43247-024-01917-3
- 1030 VanderWeele, T. J., & Mathur, M. B. (2019, March). SOME DESIRABLE PROP-
 1031 ERTIES OF THE BONFERRONI CORRECTION: IS THE BONFERRONI
 1032 CORRECTION REALLY SO BAD? *American Journal of Epidemiology*,
 1033 188(3), 617–618. Retrieved 2025-08-26, from <https://doi.org/10.1093/aje/kwy250> doi: 10.1093/aje/kwy250
- 1034 Visser, A. W. (2025, August). Sequestration by the biological carbon
 1035 pump: Do we really know what we are talking about? *Limnology and
 1036 Oceanography Letters*, n/a(n/a). Retrieved 2025-08-14, from <https://onlinelibrary.wiley.com/doi/abs/10.1002/1ol2.70053> (.eprint:
 1037 <https://aslopubs.onlinelibrary.wiley.com/doi/pdf/10.1002/1ol2.70053>) doi:
 1038 10.1002/1ol2.70053
- 1039 Volk, T., & Hoffert, M. I. (1985). Ocean Carbon Pumps: Analysis of Relative
 1040 Strengths and Efficiencies in Ocean-Driven Atmospheric CO₂ Changes. In *The
 1041 Carbon Cycle and Atmospheric CO₂: Natural Variations Archean to Present*
 1042 (pp. 99–110). American Geophysical Union (AGU). Retrieved 2025-02-04,
 1043 from <https://onlinelibrary.wiley.com/doi/abs/10.1029/GM032p0099>
 1044 (.eprint: <https://onlinelibrary.wiley.com/doi/pdf/10.1029/GM032p0099>) doi:
 1045 10.1029/GM032p0099
- 1046 Wahba, G. (1981, March). Spline Interpolation and Smoothing on the Sphere. *SIAM
 1047 Journal on Scientific and Statistical Computing*, 2(1), 5–16. Retrieved 2024-
 1048 11-09, from <https://pubs.siam.org/doi/abs/10.1137/0902002> (Pub-
 1049 lisher: Society for Industrial and Applied Mathematics) doi: 10.1137/0902002
- 1050 Wang, W.-L., Fu, W., Le Moigne, F. A. C., Letscher, R. T., Liu, Y., Tang, J.-M., &
 1051 Primeau, F. W. (2023, December). Biological carbon pump estimate based
 1052 on multidecadal hydrographic data. *Nature*, 624(7992), 579–585. Retrieved
 1053 2025-07-02, from <https://www.nature.com/articles/s41586-023-06772-4>
 1054 (Publisher: Nature Publishing Group) doi: 10.1038/s41586-023-06772-4
- 1055 Wickham, H., Averick, M., Bryan, J., Chang, W., McGowan, L. D., François, R.,
 1056 ... Yutani, H. (2019). Welcome to the tidyverse. *Journal of Open Source
 1057 Software*, 4(43), 1686. doi: 10.21105/joss.01686
- 1058 Wong, A. P. S., Wijffels, S. E., Riser, S. C., Pouliquen, S., Hosoda, S., Roemmich,
 1059 D., ... Park, H.-M. (2020, September). Argo Data 1999–2019: Two Million
 1060 Temperature-Salinity Profiles and Subsurface Velocity Observations From
 1061 a Global Array of Profiling Floats. *Frontiers in Marine Science*, 7. Retrieved
 1062 2024-05-06, from <https://www.frontiersin.org/articles/10.3389/fmars.2020.00700> (Publisher: Frontiers) doi: 10.3389/fmars.2020.00700
- 1063 Wood, S. N. (2017). *Generalized Additive Models: An Introduction with R* (2nd ed.).
 1064 Chapman and Hall/CRC.
- 1065 Zhu, R., Yang, H., Li, M., Chen, Z., Ma, X., Cai, J., & Wu, L. (2024, February).
 1066 Observations reveal vertical transport induced by submesoscale front. *Scientific
 1067 Reports*, 14(1), 4407. Retrieved 2025-07-02, from <https://www.nature.com/articles/s41598-024-54940-x> (Publisher: Nature Publishing Group) doi:
 1068 10.1038/s41598-024-54940-x